Wind Energ. Sci., 5, 29–49, 2020
https://doi.org/10.5194/wes-5-29-2020

eawe european academy of wind energy
Open Access
WIND ENERGY SCIENCE

Cluster wakes impact on a far-distant offshore wind farm's power

Jörge Schneemann[1], Andreas Rott[1], Martin Dörenkämper[2], Gerald Steinfeld[1], and Martin Kühn[1]

[1]ForWind, Institute of Physics, Carl von Ossietzky University Oldenburg, Küpkersweg 70, 26129 Oldenburg, Germany
[2]Fraunhofer Institute for Wind Energy Systems, Küpkersweg 70, 26129 Oldenburg, Germany

Correspondence: Jörge Schneemann [redacted]@uol.de)

Received: 5 July 2019 – Discussion started: 7 August 2019
Revised: 14 November 2019 – Accepted: 19 November 2019 – Published: 3 January 2020

Abstract. Our aim with this paper was the analysis of the influence of offshore cluster wakes on the power of a far-distant wind farm. We measured cluster wakes with long-range Doppler light detection and ranging (lidar) and satellite synthetic aperture radar (SAR) in different atmospheric stabilities and analysed their impact on the 400 MW offshore wind farm Global Tech I in the German North Sea using supervisory control and data acquisition (SCADA) power data. Our results showed clear wind speed deficits that can be related to the wakes of wind farm clusters up to 55 km upstream in stable and weakly unstable stratified boundary layers resulting in a clear reduction in power production. We discussed the influence of cluster wakes on the power production of a far-distant wind farm, cluster wake characteristics and methods for cluster wake monitoring. In conclusion, we proved the existence of wake shadowing effects with resulting power losses up to 55 km downstream and encouraged further investigations on far-reaching wake shadowing effects for optimized areal planning and reduced uncertainties in offshore wind power resource assessment.

1 Introduction

Wind energy utilization at sea is an increasingly important part for the transition of the mainly fossil-based energy system towards renewable electricity generation. By the end of 2018 offshore wind turbines with a capacity of 6382 MW were installed in German waters, 21 750 MW worldwide. A massive expansion of offshore wind energy utilization is expected in many countries. Germany alone aims at an installed capacity of 15 GW by the year 2030 (Mackensen, 2019). Most of this capacity will be installed in the North Sea and Baltic Sea mainly in large wind farm clusters. A wind farm cluster typically consists of several wind farms in the direct vicinity, often operated by different parties and featuring different wind turbine types and geometries. Here, we call a large accumulation of more than a hundred wind turbines a cluster.

Wind turbines extract energy from the atmosphere forming regions of reduced wind speed, so called wakes, behind them. Wakes of single wind turbines merge to a wind farm or cluster wake (e.g. Nygaard, 2014). We use the term cluster wake for the merged wakes of a large number of wind turbines of either the same or different type with no individual wind turbine wake identifiable anymore. Downstream turbines within a wind farm (e.g. Barthelmie and Jensen, 2010) and in neighbouring downstream clusters (e.g. Nygaard and Hansen, 2016) experience reduced wind speeds and reduced power generation caused by wake shadowing effects. With a rising offshore wind energy utilization, cluster wake shadowing effects will occur to an increasing degree, leading to power losses and uncertainties in offshore wind resource assessment.

Wind turbine wakes were subject of intensive research in the last decade. Wake measurements were mainly performed using the remote-sensing technique Doppler lidar (e.g. Aitken et al., 2014; Trabucchi et al., 2017; Bodini et al., 2017; Fuertes et al., 2018; Beck and Kühn, 2019), power analysis on the basis of SCADA data (e.g. Barthelmie and Jensen, 2010) or Doppler radar (e.g. Hirth et al., 2014). Fur-

thermore, several numerical studies investigated wind turbine wakes using large eddy simulation (LES) (e.g. Churchfield et al., 2012; Abkar and Porté-Agel, 2015; Dörenkämper et al., 2015b; Lignarolo et al., 2016; Vollmer et al., 2016). In an unstable atmosphere, e.g. in cold air over warm water, vertical turbulence leads to a well mixed boundary layer and causes a faster wake recovery. In stable conditions, e.g. in warm air over cold water, wake deficits can last far downstream. Hansen et al. (2011), Dörenkämper et al. (2015b) and Lee et al. (2018) investigated wake recovery with respect to atmospheric stability and found an increased length of wakes in stable stratification. Optimized wind farm layouts on the basis of the prevailing wind rose and stability distribution to reduce wake effects are commonly used (e.g. Emeis, 2009; Turner et al., 2014; Schmidt and Stoevesandt, 2015).

Cluster wakes are recently coming into the scientific focus with an increased offshore wind energy utilization. Due to the large dimensions of cluster wakes experimental investigations have been made with measurement systems capable of covering large areas like satellite synthetic aperture radar (SAR) (e.g. Hasager et al., 2015), research aircraft (e.g. Platis et al., 2018) and Doppler radar (e.g. Nygaard and Newcombe, 2018). Numerical studies were carried out by implementing wind farms in mesoscale models (e.g. Fitch et al., 2012; Volker et al., 2015). Wakes of large offshore wind farm clusters over distances of more than 10 km were first observed using data from satellite SAR (Christiansen and Hasager, 2005). Li and Lehner (2013) and Hasager et al. (2015) analysed offshore wind farm wakes using SAR images and compared the long, visible wakes to results of mesoscale models. Nygaard and Hansen (2016) analysed the power production of an offshore wind farm before and after the commissioning of a wind farm located 3 km to the west on the basis of SCADA data and discovered power losses caused by wakes of the upstream wind farm in the first rows of the downstream wind farm. Nygaard and Newcombe (2018) used dual Doppler wind radar to measure the inflow and the wake of an offshore wind farm and found wind speed deficits up to the maximal achievable downstream distance of 17 km possible with the used setup. They analysed a case with steady wind direction and speed and observed the cluster wake for over 1 h; stability information was not available. Platis et al. (2018) used in situ measurements taken with a research aircraft at hub height behind offshore wind farm clusters in the German North Sea and identified wakes with lengths of up to 55 km under stable atmospheric conditions, up to 35 km in neutral conditions and up to 10 km in unstable conditions. Siedersleben et al. (2018b) used the same flight measurements as Platis et al. (2018) to evaluate a wind farm parametrization (Fitch et al., 2012) in the numerical Weather Research and Forecasting model (WRF) that is well established in wind energy applications (e.g. Pryor et al., 2018b; Witha et al., 2019; Dörenkämper et al., 2015a). Additionally they presented an analysis of aircraft wake measurements in five different heights 5 km downwind of the cluster. The wake deficit existed in all considered height levels, also 50 m above the upper tip height of the rotor. Siedersleben et al. (2018a) investigated the micro-meteorological consequences of cluster wakes due to mixing effects in the atmosphere using the flight measurements from Platis et al. (2018). Pryor et al. (2018a) evaluated the downstream impact of large onshore wind farms in North America using the wind farm parametrization by Fitch et al. (2012) in convection-permitting mesoscale WRF simulations. Lundquist et al. (2019) analysed the physical, economic and legal consequences of wake effects between large onshore wind farms with sizes of more than a hundred megawatt each.

Wind farm cluster wakes in the far field of more than 20 km downstream have not been measured over longer periods. Satellite SAR just offers the possibility to take snapshots of the wind field. Doppler radar has been deployed on the coast monitoring a nearshore wind farm (Nygaard and Newcombe, 2018) but not in an offshore wind farm to use the full measurement range for wake analysis. Doppler lidar, which successfully monitored wind turbine wakes, was considered not to be able to achieve the measurement range needed to investigate full cluster wakes. Furthermore, the influence of cluster wakes on the power production of far downstream wind farms has not been analysed. The influence of atmospheric stability on the development and recovery of cluster wakes has not been studied in detail.

The objective of this paper is to analyse whether offshore cluster wakes have a significant and continuous influence on the power generation of a far downstream wind farm and how this influence depends on atmospheric stability. For this purpose we investigated two exemplary cases of cluster wakes approaching the 400 MW wind farm Global Tech I in the North Sea during situations with different atmospheric stabilities by means of four synchronized data sets, namely

1. large-area satellite SAR wind data,
2. continuous platform-based long-range Doppler lidar wind monitoring,
3. operational data of the wind farm Global Tech I and
4. meteorological measurements for atmospheric stability characterization.

We follow Platis et al. (2018) in their definition of the cluster wake deficit as the difference in the wind speeds from the manually selected wake region and a neighbouring free-flow region since the inflow wind speed of the wake generating cluster as reference is typically not known. Furthermore, regional and temporal differences in the wind field distort a comparison of the far-distant points in front of and far behind a cluster. Therefore, the adjacent regions in and aside the wakes are compared. Wake and free-flow regions are identified manually in this analysis.

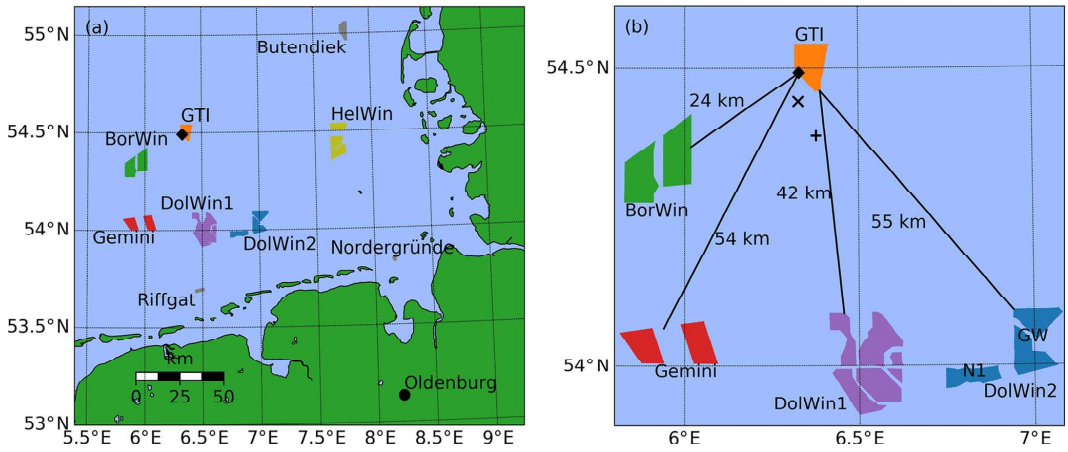

Figure 1. **(a)** Overview of the considered area in the southern North Sea with wind farms and clusters shown. **(b)** Close view on GT I and neighbouring wind farm clusters. The position of the lidar in GT I on turbine GT58 (filled ⋄) and the offshore substation (OSS) "Hohe See" (×) and the transformer platform "BorWin gamma" (+) are marked; distances to upstream clusters are also shown. We measured wakes of all clusters in **(b)** and exemplary present the wakes of the BorWin and the DolWin2 clusters in this work. Information on the wind farms and full names are listed in Table 1.

The paper is structured as follows. Section 2 introduces the experimental setup in the North Sea; measurements taken with lidar, SAR and meteorological sensors; and data processing. Section 3 presents two exemplary cluster wake cases affecting the wind farm Global Tech I. In Sect. 4 we discuss the influence of cluster wakes on the power production of a far downstream wind farm as well as cluster wake characteristics and methods for cluster wake monitoring. Section 5 concludes on the findings and closes the paper.

2 Methods

In this study different data sources have been used: meteorological measurements, wind farm production data (supervisory control and data acquisition, SCADA) and remote-sensing data from a Doppler lidar (light detection and ranging) measurement campaign, and satellite SAR (synthetic aperture radar) data. A description of these data sources is given in this section. Our measurement campaign started in late July 2018 and was planned to last 1 year. The measurements we present in this paper were taken on 11 October 2018 and 6 February 2019. All measurement data in this study were recorded in Coordinated Universal Time (UTC).

2.1 Wind farms and SCADA data

As of early 2019, several offshore wind farms were installed mainly in clusters in the German and Dutch North Sea. Focus of this work is on the effects on the 400 MW wind farm Global Tech I (GT I), which is one of the world's most distant offshore wind farms with a coastal distance of more than 100 km. We analyse the impact of two large wind farm clusters, namely the 802 MW "BorWin" cluster located about

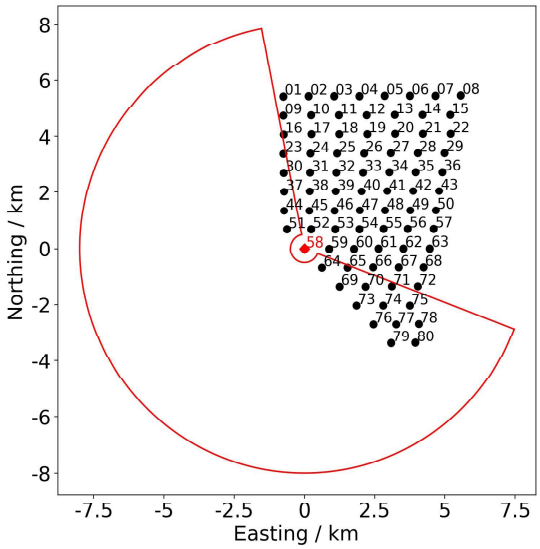

Figure 2. Layout of the wind farm Global Tech I with turbine numbers. The turbine GT58, where we positioned the lidar, is marked in red (⋄). The achievable sector for lidar measurements is drawn.

25 km southwest and the 914 MW "DolWin2" cluster 55 km southeast on the wind farm GT I.

Figure 1 gives an overview of the region around GT I while Fig. 2 displays its layout.

All coordinates in maps we show in the following, except Fig. 1, were transferred to the Gauss Krüger coordinate system and the origin was shifted to the lidar position at turbine GT58 in GT I (Fig. 2). Table 1 summarizes the main characteristics of the wind farms and clusters in the region. In the direct southwestern vicinity of GT I, the associated wind farms Hohe See and Albatros were under construction

Table 1. Overview of offshore wind farms considered in this work (as of June 2019). The wind farms Borkum Riffgrund 2 (Orsted, 2018) and "Merkur Offshore" (Merkur Offshore, 2018) were in the commissioning phase and partly fed into the grid during our measurements; therefore, they are marked with smaller symbols in the relevant plots in this paper. D: rotor diameter, h_H: hub height, P_r: rated power per turbine, No.: number of turbines per wind farm, ΣP_r: rated power of wind farm. The numbers for the hub height are related to different reference levels, namely lowest astronomical tide (LAT), mean sea level (MSL) or just "over water". These differences are not further considered here since the difference between LAT and MSL is typically around 2 m in the North Sea.

Name	Short	Turbine	D (m)	h_H (m)	P_r (MW)	No.	ΣP_r (MW)
Global Tech I	GT I	AD 5–116	116	92	5.0	80	400
BorWin Cluster (802 MW)							
BARD Offshore 1	BO1	BARD 5.0	122	90	5.0	80	400
Veja Mate	VM	SWT-6.0-154	154	103	6.0	67	402
Gemini Cluster (600 MW)							
Buitengaats	BG	SWT-4.0-130	130	89	4.0	75	300
Zee Energie	ZE	SWT-4.0-130	130	89	4.0	75	300
DolWin 1 Cluster (1416 MW)							
Trianel Windpak Borkum	TWB	AD 5–116	116	92	5.0	40	200
alpha ventus	av	AD 5–116	116	90	5.0	6	30
		5M	126	92	5.0	6	30
Borkum Riffgrund 1	BR1	SWT-4.0-120	120	87	4.0	78	312
Borkum Riffgrund 2	BR2	V164-8.0	164	111	8.0	56	448
Merkur Offshore	MO	Haliade 150-6	150	103	6.0	66	396
DolWin 2 Cluster (914 MW)							
Nordsee One	N1	6.2M-126	126	90	6.15	54	332
Gode Wind 1 + 2	GW	SWT-6.0-154	154	110	6.0	97	582

during the period of our measurement campaign with several transition pieces and a substation but no wind turbine towers installed. The first turbine was erected on 6 April 2019 (EnBW, 2019). The position of the Hohe See offshore substation (OSS) is marked in the following plots (×). The installation of the 900 MW high-voltage direct current (HVDC) platform BorWin gamma in the southeast corner of Hohe See was completed on 11 October 2018 (Petrofac, 2018); we also mark its position (+).

For the wind farm GT I, 10 min averaged SCADA data were available during the period of the measurements. Data of turbines in normal operation were considered; turbines with curtailed power below rated power were excluded from the analysis based on a SCADA status flag, a curtailment signal and consideration of pitch angles. For the wind farms BARD Offshore 1, Gode Wind 1 + 2 and Nordsee One we obtained hourly production data from Fraunhofer ISE (2019) and checked the operational status.

We analyse wind turbine power differences using the z score

$$z_{P_i} = \frac{P_i - \overline{P_{up}}}{\sigma_{P_{up}}} \quad (1)$$

with z_{P_i} being the difference in the ith turbine's power P_i and the mean power of the turbines in the first row facing the wind direction (upstream turbines) $\overline{P_{up}}$ normalized with the standard deviation of the power of the upstream turbines $\sigma_{P_{up}}$ within the considered time span. Advection through the farm is not considered. We use the upstream turbines to calculate the z score instead of the turbines of the whole farm to avoid distortion by inner-farm wake effects.

2.2 Lidar measurements

We used a scanning long-range Doppler lidar system of type Leosphere Windcube 200S (serial no. WLS200S-024) in this study. The lidar system emits laser pulses into the atmosphere and analyses the light backscattered by aerosols for a Doppler shift proportional to the radial wind velocity in beam direction v_r. The lidar is able to process wind speed information in > 200 different ranges on the beam called range gates. For each range gate, the radial wind speed v_r and the carrier-to-noise ratio (CNR) as a measure of the signal quality are stored. The lidar's scanner is able to point the beam in any desired direction in the hemisphere above and partly below the device.

We installed the lidar system on the transition piece (TP) of wind turbine GT58 in GT I (filled ◇ in Figs. 1 and 2). The height of its scanner was approximately 24.6 m a.m.s.l. (above mean sea level), 67.0 m below hub height and 9.0 m below lower blade tip height of the turbine. Figure 3 displays a picture of the lidar installed in GT I.

Table 2. Overview of the different settings for the lidar plan position indicator (PPI) scans. Both scenarios covered different sectors of 150° width. Range gates are listed as minimal range : spacing : maximal range. Range gates are also referred to as "measurement points" in the following.

Scenario	Pulse length (ns)	Acquisition time (s)	$\dot{\varphi}$ (° s^{-1})	Scan duration (s)	Range gates (m)
A	400	8.0	0.25	600	1000 : 50 : 12 000
B	400	2.0	1.0	150	500 : 35 : 8000

Figure 3. Lidar system Windcube 200S on the transition piece of wind turbine GT58 in the offshore wind farm Global Tech I. On the right side of the image the tower of the turbine is visible while turbine GT51 northwest of GT58 can be seen in the background (cf. GT I layout in Fig. 2) (Stephan Voß, ForWind).

The lidar performed horizontal plan position indicator (PPI) scans (elevation angle φ was 0°) with continuous scanner movement in different azimuthal sectors of 150° width upstream with two different settings, A and B, as listed in Table 2. We started with the slower scenario A aiming for a high measurement range. Later we optimized the measurements using scenario B, being 4 times faster and achieving similar ranges. In both scenarios the laser beam is scanned over an angle of 2° per measurement leading to spatial averaging perpendicular to the line of sight direction. After performing a scan, the lidar needs a few seconds to reset and start the next scan. Every few hours it performs a homing procedure of the scanner to assure precise orientation. The laser pulse length used in both scenarios was 400 ns, leading to a probe volume of approximately 70 m in the beam direction. The range gate spacing is listed in Table 2.

The offset in the azimuthal direction between geographic north and the lidar's north was corrected by scanning distant wind turbines in GT I with known positions ("hard targeting"). The resulting error in the azimuthal orientation $\Delta\varphi$ was smaller than 0.1° and is therefore neglected.

The lidar was well aligned on the pitch and roll axis; errors were checked using the method of sea surface levelling (Rott et al., 2017). The resulting maximal error in the elevation $\Delta\vartheta$ was less than 0.1°. An additional error in the elevation angle of the lidar measurement occurs from a small movement of the TP due to the thrust on the rotor with a maximum of 0.1°.

When regarding the height of the measurement locations, the curvature of the earth must be taken into account for the ranges achieved. The error introduced raises quadratically with range and reaches $\Delta h_8 = 5.02$ m for a distance of 8 km and of $\Delta h_{10} = 7.85$ m for a distance of 10 km. The measurement errors we describe here can be neglected for the mainly qualitative analysis in this work.

2.3 Lidar data processing

Lidar scans were individually filtered on CNR minimal and maximal thresholds, a maximum range, and a minimal data density in the v_r–CNR plane (similar to Beck and Kühn, 2017). For each PPI scan, the mean wind direction was determined by fitting a cosine function to all radial speeds v_r of the scan over their azimuth angles φ. All v_r were then transformed back to the absolute wind speed v_a in mean wind direction assuming the perpendicular wind component to vanish using

$$v_a = v_r / \cos(\varphi_{diff}) \quad (2)$$

with φ_{diff} being the difference angle between the beam direction and the mean wind direction. Sectors with measurement ranges almost perpendicular to the wind direction ($|\varphi_{diff}| > 75°$) were excluded from the analysis because of an increasing error due to an overestimation of flow components perpendicular to the wind direction. We plot single lidar scans on their original polar grid. To obtain averaged lidar wind fields, we transferred the v_a-lidar data of each regarded scan to a Cartesian grid with a resolution of 50 m × 50 m, triangulating the data points and on each triangle performing linear barycentric interpolation to the grid points. We then calculated the cubic (or power) average on each grid point. Due to slightly changing wind directions in the averaging interval, points at the border of the scans were just included in the

Table 3. Classification of atmospheric stability as suggested by Sorbjan and Grachev (2010).

Stability category	Range
Very stable	$0.6 < \zeta < 2.0$
Stable	$0.2 < \zeta < 0.6$
Weakly stable	$0.02 < \zeta < 0.2$
Near neutral	$-0.02 < \zeta < 0.02$
Weakly unstable	$-0.2 < \zeta < -0.02$
Unstable	$-0.6 < \zeta < -0.2$
Very unstable	$-2.0 < \zeta < -0.6$

further analysis if no scan (scenario A) or less than 10 scans (scenario B) did not contribute at the grid point.

2.4 Atmospheric stability and meteorological data

Meteorological measurements of atmospheric stability are uncommon in offshore wind farms. Different methods for the derivation of stability exist (see Rodrigo et al., 2015 for an overview). We applied the *bulk Richardson method from profile measurements* according to Emeis (2018) based on the tropical observations of Grachev and Fairall (1997). We used the wind speed v_{TP}, the temperature T_{TP} on the height of the transition piece z_{TP}, and the difference in the virtual potential temperatures at the height of the TP and at sea level, $\Delta\Theta_{\mathrm{v}} = \Theta_{\mathrm{v,TP}} - \Theta_{\mathrm{v,SST}}$ (see Appendix A), to derive the dimensionless bulk Richardson number

$$Ri_{\mathrm{b}} = \frac{g}{\Theta_{\mathrm{v,TP}}} \frac{z_{\mathrm{TP}} \Delta\Theta_{\mathrm{v}}}{v_{\mathrm{TP}}^2}, \tag{3}$$

where g is the gravity acceleration. The dimensionless stability parameter,

$$\zeta = \begin{cases} \frac{10 Ri_{\mathrm{b}}}{1 - 5 Ri_{\mathrm{b}}} & Ri_{\mathrm{b}} > 0, \\ 10 Ri_{\mathrm{b}} & Ri_{\mathrm{b}} \leq 0, \end{cases} \tag{4}$$

and the stability classification in Table 3 were chosen for stability categorization.

To be able to estimate ζ, we operated sensors for air pressure (Vaisala PTB330) as well as temperature and relative humidity (Vaisala HMP155) on the TP of turbine GT58. In one case (see Sect. 3.2.1) we used meteorological measurements from the nacelle of turbine GT58 provided by the wind farm operator as a second source of data to derive the stability parameter at height of the nacelle ζ_{nac} using the same methodology as described above. A buoy for the measurement of the sea surface temperature T_{SST} was available from 9 August 2018 until 31 January 2019. We compared the measurements with the OSTIA data set (Donlon et al., 2012), both resampled to a 30 min interval (mean values for the buoy data, linear interpolation for the daily available OSTIA data set), and found a mean difference of 0.19 K. Since the buoy was not available during the whole lidar measurement campaign, we use T_{SST} from the OSTIA data set to derive ζ. The wind speed on the height of the TP, v_{TP}, for the purpose of atmospheric stability analysis was calculated from horizontal lidar PPI scans as described in Sect. 2.3 using data with a measurement range less than 3000 m. These measurements took place within the approaching cluster wakes, when present. This influences the calculation of the stability parameter but we see the wake as part of the inflow and do not try to correct for it. We averaged meteorological measurements to 30 min intervals. Table 4 shows an overview of the available meteorological data.

For a comparison of the potential power P_{pot} in the wind with the power harvested by free-flow turbines, we had to transfer wind speeds from measurement heights ($z_{\mathrm{SAR}} = 10$ m, $z_{\mathrm{TP}} = 24.6$ m) to hub height $z_{\mathrm{hub}} = 91.6$ m. Following Emeis (2018), we used the logarithmic wind profile

$$u(z) = \frac{u_*}{\kappa} \cdot \left(\ln \frac{z}{z_0} - \Psi_m(z/L) \right) \tag{5}$$

with a correction function $\Psi_m(z/L)$ to account for the atmospheric stability to calculate the vertical wind profile. We used mesoscale data with a setup very similar to the production runs of the New European Wind Atlas (NEWA; see Witha et al., 2019; NEWA, 2019) internally deriving the roughness length z_0 using Charnock's relation. We obtained the Obukhov length L from the stability parameter $\zeta = z_{\mathrm{TP}}/L$. The von Kármán constant reads as $\kappa = 0.4$. The friction velocity u_* was then calculated for the given pair of wind speed and height, e.g. z_{TP} and u_{TP} from Eq. (5). The wind speed on hub height was afterwards converted to the theoretical potential power P_{pot} using a power curve $P_{\mathrm{est}}(v) = c \cdot v^3$ with the constant c derived from power data in the partial load range. We do not curtail P_{pot} at rated wind speeds allowing it to be larger than rated power.

2.5 SAR wind data

Satellite SAR remotely measures the roughness of the sea surface. Using a geophysical model to estimate wind direction, wind speeds over the ocean can be derived. In this work, we use publicly available already processed wind data from the Copernicus SAR satellite Sentinel-1A. The algorithm for wind field processing is described in Mouche (2011), an overview of its performance is given in ESA (2019) and the data product including quality flags is described in Vincent et al. (2019). Wind data at 10 m height are processed on a grid with a spatial resolution of 1 km × 1 km. Wind speed estimates are in range from 0 to 25 m s^{-1} with a root mean square error (RMSE) smaller than 2.0 m s^{-1} and wind direction estimates have an RMSE below 30°. The spatial coverage of the SAR images and the processed wind fields is 170 km × 80 km minimum with a revisit time of the order of days. A quality flag for the wind estimate (*owiWindQuality*, 0: high quality, 1: medium quality, 2: low quality, 3: bad quality; see Vincent et al., 2019) is provided within the data

Table 4. Overview of the available meteorological quantities to derive the stability parameter ζ. Availabilities disregard shorter data gaps. If no end time is stated, measurements are ongoing with date of 1 August 2019. Additional data from mesoscale simulations similar to the New European Wind Atlas (NEWA) data set were available but not listed in this table.

Quantity	Symbol	Sensor or source	Height	Availability period
Air temperature	T_{TP}	HMP155	$z_{TP} = 24.6$ m a.m.s.l.	23 Jul 2018
Air humidity	RH_{TP}	HMP155	$z_{TP} = 24.6$ m a.m.s.l.	23 Jul 2018
Air pressure	P_{TP}	PTB330	$z_{TP} = 24.6$ m a.m.s.l.	23 Jul 2018
Wind speed	$v_{TP,lidar}$	lidar PPI scans	$z_{TP} = 24.6$ m a.m.s.l.	17 Aug 2018 (dep. on scan scenario)
Sea surface temperature	$T_{SST,buoy}$	buoy next to GT58	sea surface	9 Aug 2018–31 Jan 2019
Sea surface temperature	$T_{SST,OSTIA}$	OSTIA data set	sea surface	2018–2019

product. We use data with a quality flag ≤ 2. For the calculation of the potential power on hub height (see Sect. 2.4), we added constant wind speed values within the measurement accuracy to the SAR wind data to match the actual power production.

3 Results

In this section we present an analysis of wake situations of the BorWin cluster on 6 February 2019 and of the DolWin2 cluster on 11 October 2018 based on Sentinel-1 SAR wind data, lidar measurements and SCADA power data of the wind farm GT I.

3.1 BorWin cluster wake on 6 February 2019

The BorWin cluster is located approximately 24 km upwind of GT I in southwesterly direction. We measured wakes from the cluster approaching GT I in stable stratified situations during our measurement campaign. Here we present a stably stratified situation in late winter 2018/2019 with low variation in the wind direction allowing us to analyse lidar scans of the same situation over a period of a couple of hours.

3.1.1 Meteorological conditions

In Fig. 4 we plot the measured wind speed and direction, air pressure, temperature and humidity, and the sea surface temperature from the OSTIA data set and the derived stability parameter ζ during 6 February 2019. On that day the frontal system of a cyclone southwest of Iceland crossed the German Bight. The warm front passed GT I in the morning, bringing air temperatures of about 6.9 °C in the warm sector over the 6.1 °C cold sea stabilizing the boundary layer. With decreasing humidity and disappearing fog, good lidar availability was achieved starting at approximately 10:00 UTC (short humid or foggy period of bad measurements around 12:00 UTC) with clear wakes of the BorWin cluster visible in the lidar scans. In the afternoon we choose a period with relatively constant wind direction from 13:35 to 16:12 UTC for analysing the averaged wake effects over a longer period of about 2.5 h. The period with stable stratification ended with the passage of the cold front at approximately 17:15 UTC.

3.1.2 SAR wind data

Figure 5 displays the analysis of a wind field derived from the measurement of the Copernicus satellite Sentinel-1A, which passed the German Bight at the end of the stable stratified period on 6 February 2019 as an overview of the wind field in the region around GT I. The wake of the BorWin cluster is clearly visible and extends approximately 24 km downstream until it partially hits the wind farm GT I. Further downstream of GT I an even higher wake deficit of the merged wakes of the BorWin cluster and GT I can be observed. The virtual wake cut (Fig. 5c) reveals a sharp transition from higher to lower wind speeds at the edge of the wake; a deficit in the SAR wind speed of 0.9 m s^{-1} is observed. Since the wake just partially hits GT I, it separates the farm into two regions: one in free flow and one affected by the wake. The turbines in free flow in the northwestern and southern corner of GT I produce significantly more power ($> 2\sigma_P$) than the first upstream row of turbines produce on average (Fig. 5b). We confirm this result with the comparison of the 10 min power of the upstream-row turbines with the potential power on hub height derived from the inflow wind speed (Fig. 5d) which agrees well. Within the wake-affected region in GT I, typical inner-farm wake effects are visible through a power decrease in downstream direction (e.g. Barthelmie and Jensen, 2010, Fig. 5b) which are different in the northern and southern parts of the farm due to different turbine spacings in wind direction.

3.1.3 Lidar wind fields

In Fig. 6 we present the analysis of a single lidar scan of the inflow of GT I. We observe a clear edge between high wind speeds in the undisturbed flow and lower wind speeds in the wake of the BorWin cluster, causing a clear separation of power production in the wind farm GT I in a free-flow and a wake region (Fig. 6b). The virtual wake cut in Fig. 6c illustrates the sharp transition region of just a few hundred metres width and highlights the wake deficit of 3.9 m s^{-1} or

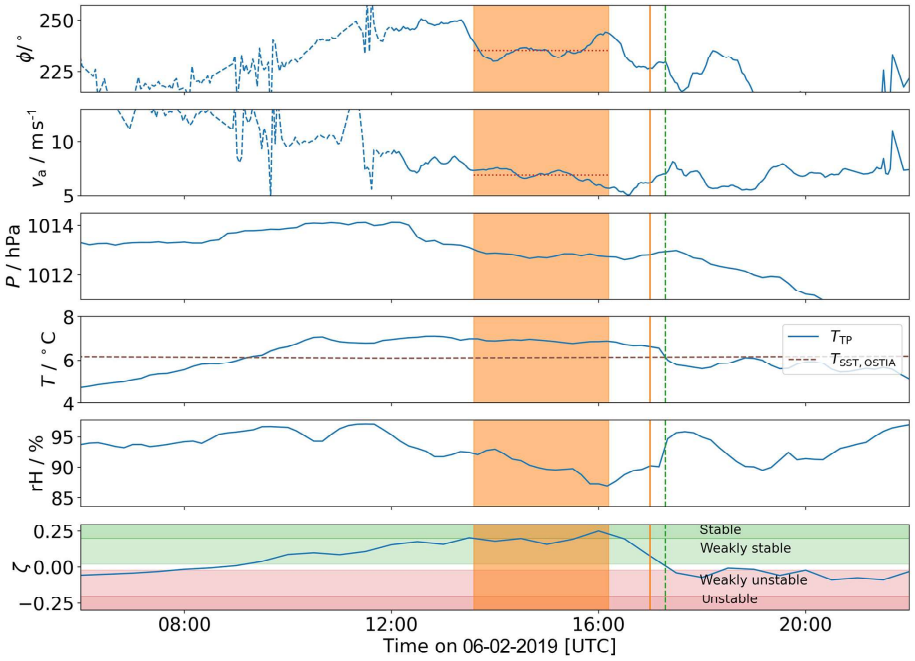

Figure 4. Meteorological data at the lidar location on the height of the TP (24.6 m a.m.s.l.) of turbine GT58 on 6 February 2019. Top to bottom: wind direction $\phi_{TP,lidar}$, wind speed $v_{TP,lidar}$, air pressure P_{TP}, air and sea surface temperature T_{TP} and $T_{SST,OSTIA}$, relative humidity RH_{TP}, and the dimensionless stability parameter ζ_{TP}. Measurement times are marked as follows: vertical dashed line represents the SAR image (Fig. 5), vertical solid line represents the single lidar scan (Fig. 6), and shaded interval represents the averaged lidar wind field (Fig. 7). Mean wind speed and direction in the averaged lidar interval are marked by red horizontal dotted lines. Dashed lines in wind speed and direction indicate moist or foggy periods with reduced lidar data availability.

40.5 %. The potential power on hub height derived from the inflow wind speed corresponds well with the power generated by the upstream row of turbines in the regarded 10 min interval (Fig. 6d). The two northerly upstream turbines are in the region of free flow and produce, with $> 2\sigma_P$, significantly more power than the turbines being influenced by the BorWin wake.

In Fig. 7 we present an averaged lidar wind field calculated from 60 consecutive scans like the one in Fig. 6 in a period of approximately 157 min with relatively constant wind direction (see shaded areas in Fig. 4) to demonstrate the steadiness of the BorWin wake and its influence on power production. The wind speed along the virtual cut through the wind field in Fig. 7c reveals a strong average wake deficit of 2.3 m s^{-1}, equivalent to 24.7 %. The transition region from wake flow to free flow is about 3 km wide resulting from the small changes in wind direction and thus the slightly different positions of the wake during the averaging time. Aside from the clear visible northerly edge of the BorWin wake, the southerly edge can be observed in the southerly corner of the lidar wind field and correspondingly in the wake cut (Fig. 7c). Wind speeds recover on both sides of the wake to similar values just above 9 m s^{-1}. The average power of the GT I turbines reveals a clear reduction in the wake-affected region (Fig. 7b). The turbines in free flow produce ($> 2\sigma_P$) above the average. Comparing the potential power on hub height along the wake cut together with the average power of the upstream-row turbines (Fig. 7d), we find a slight overestimation of the potential power in the wake region and an overestimated increase in the turbine power in the transition region. The position of the transition onset in the estimated power from the wind field and the measured power from the turbines agree well.

3.2 DolWin2 cluster wake on 11 October 2018

The DolWin2 cluster is approximately 55 km upstream of GT I in southeasterly direction. We regularly have indications in our measurements for wakes from the cluster approaching GT I in stably stratified situations. Here we present a situation in autumn 2018 with a change of stability over the course of the day. We present a single lidar scan and an averaged lidar wind field from a period with low variation in the wind direction in stable stratification. A complementary SAR scan from the morning of the day during weakly unstable stratification is available as well and analysed here.

3.2.1 Meteorological conditions

In Fig. 8 we plot the measured meteorological quantities on 11 October 2018. Since the lidar for measurements of wind speed and direction and the data of air temperature,

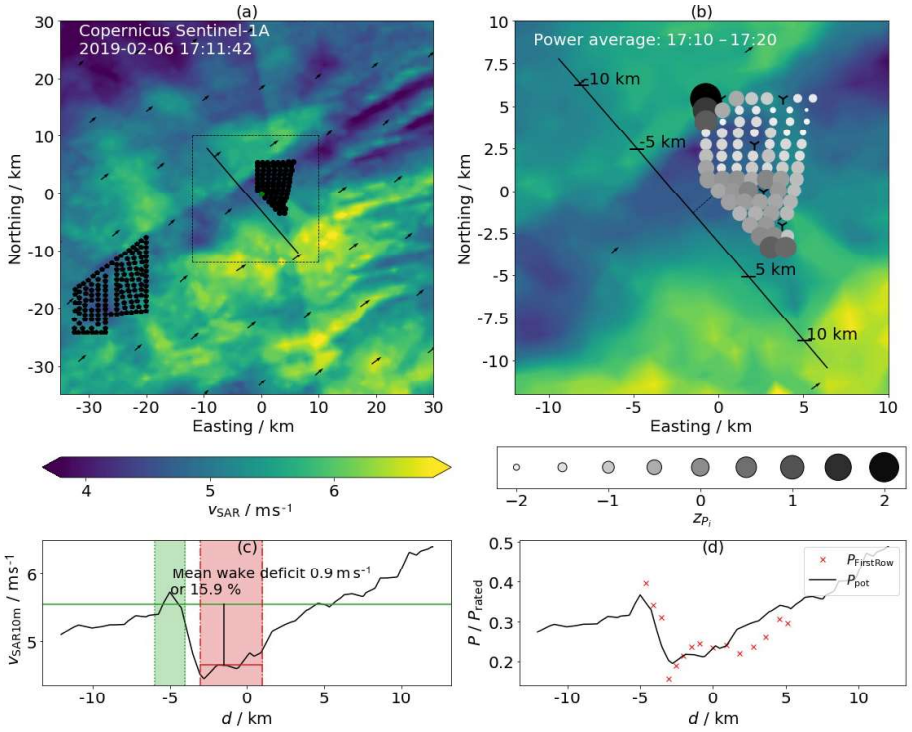

Figure 5. Sentinel-1A Ocean Wind Field (Copernicus Sentinel data (2019)), measurement taken 6 February 2019 17:11:42 UTC. **(a)** Overview of the BorWin cluster and Global Tech I. **(b)** Close look on the BorWin wake hitting GT I. The solid line marks a virtual wake cut 2000 m upstream of turbine GT58 on which the wind field is evaluated. Marked distances correspond to the x axis of **(c)** and **(d)**. The z score of the turbine power z_{P_i} (see Eq. 1) is shown in greyscale for the relevant 10 min period (17:10–17:20 UTC); markers scale with $z - z_{\min}$. Numbers of upstream turbines to calculate the z score are 1, 9, 16, 23, 30, 37, 44, 51, 58, 64, 69, 73, 76, 79, and 80. Turbines not operating the full period or operating at curtailed power are excluded and marked (Y-shaped marker). **(c)** Wind speeds along the wake cut from **(b)**. Wake and the free stream are shaded (regions selected manually). **(d)** Potential power on hub height along the wake cut (solid line) together with the power produced by the upstream turbines in GT I within the regarded 10 min interval with turbine positions projected to the wake cut. A constant value of 1.0 m s^{-1} was added to $v_{\mathrm{SAR,10\,m}}$ for the calculation.

pressure and humidity at TP height were not available during the whole day we added the mesoscale data from the New European Wind Atlas (NEWA) and measurements from the nacelle of turbine GT58 to the plots. A cyclone southwest of Iceland and a strong high-pressure area over Russia dominated the weather during the day. The North Sea was positioned in the warm sector of the cyclone between the cold front over the UK and the warm front spanning from Iceland to Norway. Southeasterly winds prevailed in the southern North Sea raising the air temperature in GT I between 12:00 and 14:00 UTC above the temperature of the still quite warm North Sea (approximately 16 °C) stabilizing the boundary layer. In the morning a shallow (weakly) unstable boundary layer of some hundred metres height occurred because the surface layer over land cooled down during the night to temperatures below sea surface temperature and moved with the prevailing flow over the sea. Aside from the stability obtained from NEWA (weakly unstable) and the nacelle measurements (unstable), this finding is further supported by temperature profiles sounded with radiosondes at the stations in Bergen (no. 10238) and Ekofisk (no. 1400) the same day. A weak inversion with temperatures of approximately 13.5 °C up to 300 m height appears in the profile at Bergen, 04:00 UTC, with a stronger temperature inversion above. At the Ekofisk site the temperature profile at 11:00 UTC shows a similar behaviour with the upper inversion being less pronounced and sunken to approximately 230 m height. This allows for dry adiabatic convection up to heights between 200 and 300 m for the prevailing sea surface temperature.

We found a good general agreement between the NEWA data and the values measured in the wind farm. Especially the derived stability parameter ζ agrees well. For the differences in the other quantities the different reference heights have to be considered. Half-hourly values of wind speed and direction from the NEWA data are not expected to cover small-scale fluctuations and to perfectly match a local measurement.

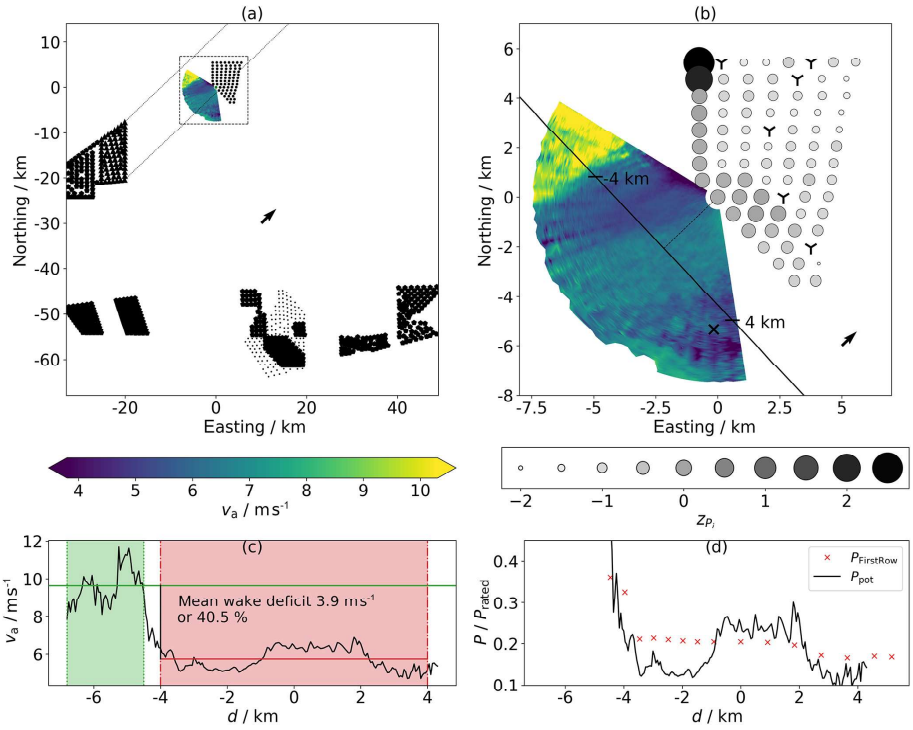

Figure 6. Lidar scan (scenario B from Table 2) on 6 February 2019 16:58–17:01 UTC: **(a)** overview of the situation in the German Bight with lines parallel to the wind direction retrieved from the lidar scan from the corners of the upstream wind farm cluster BorWin. Lidar wind speed is colour coded (left colour bar). **(b)** Close view of the lidar wind field and the wind farm GT I. The z score of the not curtailed wind turbines' power in the current 10 min interval (16:50–17:00 UTC) is in greyscale (right colour bar), curtailed or non-operating turbines are marked (Y-shaped marker). Markers scale with $z - z_{\min}$. Turbine numbers to calculate the z score as in Fig. 5. The substation Hohe See ($\times$) is marked. The solid line marks a virtual wake cut 3000 m upstream of turbine GT58 on which the wind field is evaluated and drawn in **(c)**. Areas of wake and free stream are shaded manually, the resulting wake deficit is stated. **(d)** Available power on hub height along the wake cut from **(b)** together with the power achieved from the upstream turbines in GT I with their positions projected to the wake cut.

3.2.2 SAR wind data

Figure 9a shows the wind field from the Copernicus satellite Sentinel-1A, which passed the German Bight in the morning of 11 October 2018, as an overview of the wind field in the region between GT I and the DolWin2 cluster. The stratification during the SAR snapshot was weakly unstable. Wakes of the Gemini, DolWin1 and DolWin2 clusters with lengths of at least 20, 40 and 55 km, respectively, are clearly visible. The wake originating in the DolWin2 cluster splits into two parts generated by "Gode Wind 1 + 2" (GW) and Nordsee One (N1); see Fig. 1. The GW wake extends far downstream until it hits the wind farm GT I after approximately 55 km. Further downstream a merged wake of the DolWin2 cluster and GT I can be observed extending out of the visible range after approximately 30 km. All wakes have the approximately same width as the generating cluster and become narrower downstream.

The virtual wake cut 9000 m upstream of GT58 reveals regions of different influence (Fig. 9c). On the southwest side of the cut we see a region of undisturbed flow ($d \approx -15$ km, d is the distance on the wake cut from Fig. 9c) with wind speeds decreasing towards northeast. The deficit between $-5\,\text{km} < d < 0\,\text{km}$ originates in the wake of the wind farm N1 followed by the stronger deficit at $0\,\text{km} < d < 10\,\text{km}$ of the GW wind farm. This wake deficit centrally hits GT I and affects its power production. Further east the wind speed remains approximately constant until it rises from $d > 20$ km due to regional differences in the wind field. Regarding the marked wake and free-flow regions in Fig. 9c, we observe a wake deficit of 0.6 m s^{-1} or 7.2 % in the SAR wind speed for the DolWin2 wake in 10 m height.

Differently from the wake situation of the BorWin cluster (Sect. 3.1), the wind farm GT I is affected by the DolWin wake centrally; therefore, we do not observe separated regions of power production within the farm. Nevertheless, the outer turbines on the western and northeastern corner of the wind farm produce significantly more power (2.6 and 1.7σ_P above average) than the average of the upstream row (Fig. 9b). Looking at the potential power on hub height calculated from the virtual wake cut (Fig. 9d), we find the increased power to result from the higher wind speeds at the sides of the DolWin2 wake deficit. This highlights the effect

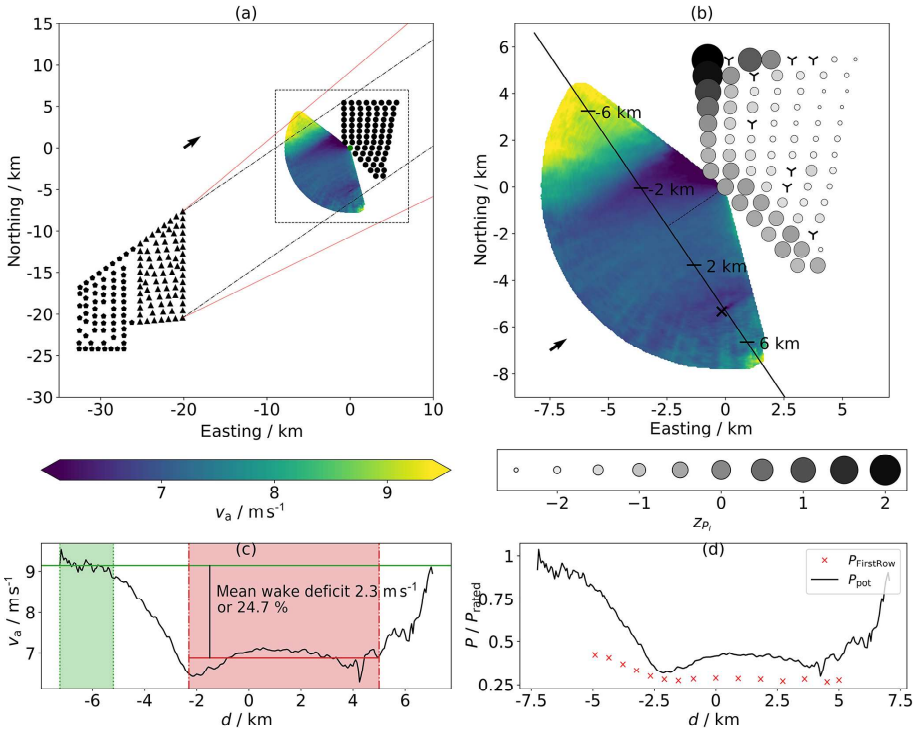

Figure 7. As in Fig. 6 but averaged over 60 consecutive lidar scans (scenario B) corresponding to a period of 157 min (13:35–16:12 UTC); power data averaged over 170 min (13:30–16:20 UTC). Red lines in **(a)** indicate minimal and maximal wind directions within the averaging interval.

of the wake on the power production even in weakly unstable conditions.

3.2.3 Lidar wind fields

In Fig. 10 we show a single lidar scan of the flow southwest of GT I. The stratification during the scan was stable (Fig. 8). We do not observe a sharp transition from wake to free-flow regions like for the BorWin wake (Fig. 6) but a steady decrease in wind speeds southwest to northeast, similar to the DolWin2 wake situation we found in the SAR data from the same morning in weakly unstable stratification (Fig. 9). Three more wakes appear in the wind field: one originating from a ship close to GT I, another one from the OSS Hohe See ($\times$) and the third from the platform BorWin gamma ($+$). The latter wake extends at least 9 km downstream.

The virtual wake cut (Fig. 10c) highlights the different flow regions with lower wind speeds near GT I. The Hohe See OSS wake is located at $d \approx -4$ km and the BorWin gamma wake between $-6\,\text{km} < d < -5.5\,\text{km}$. The wake deficit of the DolWin2 cluster amounts to 3.3 m s^{-1} or 26.4 %. Comparing the potential power in the wind field with the power produced by the turbines of the upstream row, we find most turbines producing approximately rated power (Fig. 10d). The potential power in the west of the wind farm is slightly lower than the power of the upstream turbines. Even though during this lidar scan with high wind speeds the wind farm's power is not influenced by the DolWin2 wake due to the turbines curtailing power production above rated speed, we find clear indications for wake effects with reduced wind speeds at the position of GT I 55 km downstream the DolWin2 cluster.

Figure 11 highlights the steadiness of the DolWin2 wake situation on 11 October 2018. We averaged 16 consecutive lidar scans in a period of approximately 162 min (15:44 to 18:26 UTC; cf. shaded interval in Fig. 8) with a relatively constant wind direction. As for the single lidar scan we observe the same behaviour in the wind field with a wind speed decreasing along the virtual wake cut from southwest to northeast. The wake deficits of the Hohe See OSS and BorWin gamma are clearly visible in the averaged wind field (Fig. 11c). The relative wake deficit of the DolWin2 cluster is similar for the single and the averaged lidar scans (Fig. 10). Since the average wind speed within the averaging period is smaller than that at the time of the single scan (Fig. 8), the absolute deficit is smaller, too. The course of the potential power in the wind field (Fig. 11d) is continued by the power of the upstream-rows turbines. The wake effect of the DolWin2 cluster on the power of GT I is evident. The potential power in the wind about 4 km southwest of the wind farm reaches rated wind speed.

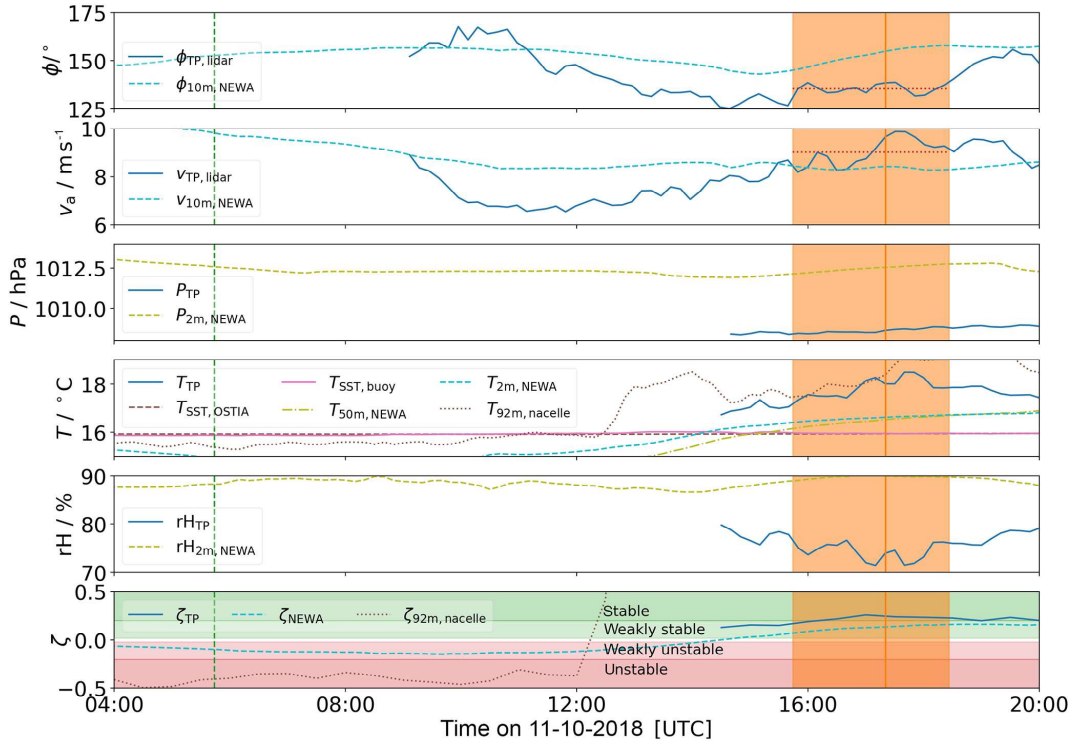

Figure 8. Meteorological data at the lidar location (turbine GT58) on 11 October 2018. Top to bottom: wind direction $\phi_{TP,lidar}$, wind speed $v_{TP,lidar}$, air pressure P_{TP}, air temperature T_{TP}, sea surface temperatures $T_{SST,OSTIA}$ and $T_{SST,buoy}$, relative humidity RH_{TP}, and the dimensionless stability parameter ζ_{TP} on the height of the TP of GT58 (24.6 m a.m.s.l.). Since the measurements are not available during the whole day, we added the 10 m wind speed $v_{10\,m,NEWA}$ and direction $\phi_{10\,m,NEWA}$, 2 and 50 m temperature $T_{2\,m,NEWA}$ and $T_{50\,m,NEWA}$ and the stability parameter ζ_{NEWA} from the NEWA data set (see Witha et al., 2019) as well as the temperature $T_{92\,m,nacelle}$ and the derived stability parameter $\zeta_{92\,m,nacelle}$ on hub height of turbine GT58. Measurement times are marked as follows: vertical dashed line represents the SAR image (Fig. 9), vertical solid line represents the single lidar scan (Fig. 10), and shaded interval represents the averaged lidar wind field (Fig. 11). Mean wind speed and direction in the averaged lidar interval are marked by red horizontal dotted lines.

4 Discussion

We found evidence of cluster wakes in the form of wind speed deficits with clear transition regions between slower wake flow and faster undisturbed flow in many lidar scans upstream of GT I for all neighbouring wind farm clusters in southeasterly to westerly wind directions, namely the DolWin2 (approximately 55 km), DolWin1 (approximately 42 km), Gemini (approximately 54 km) and BorWin (approximately 24 km) clusters. In some of the cases with available large-area SAR wind data, these alternative measurements supported the lidar cluster wake measurements. Power deficits in the wind farm agree with the wake regions found in lidar and SAR data. In this paper we present two exemplary wake cases: one for the BorWin cluster 24 km upstream and one for the DolWin2 cluster 55 km upstream, and both wake effects occurred steadily over more than 2.5 h and influenced the power production of GT I. We found cluster wakes mainly for positive values of the stability parameter ζ (stable stratification) but also for ζ slightly below zero (weakly unstable stratification, shallow boundary layer).

4.1 Influence of cluster wakes on power production of far downstream wind farms

The effect of cluster wakes on the operation of far downstream wind farms has not been investigated before. Nygaard and Hansen (2016) report about short-distance effects in the power production of wind farms in the direct vicinity (3.3 km gap) based on SCADA analysis. Nygaard and Newcombe (2018) analyse a cluster wake at hub height up to 17 km downstream a wind farm with dual Doppler radar from the coast. Platis et al. (2018) find long-reaching wake effects (wind speed difference of more than 0.1 m s^{-1} considered wakes) up to 55 km downstream in flight measurements but could not analyse their impact on distant wind farms. Here, our findings from combined satellite SAR and lidar measurements of cluster wakes existing over distances of up to 55 km downstream agree with the observation of Platis et al. (2018). Additionally, we confirm the assumption of negative effects of cluster wakes on the power production of a far downstream wind farm.

The evidence of the wake influence on wind farm power is obvious for the BorWin case where we find a clear distinc-

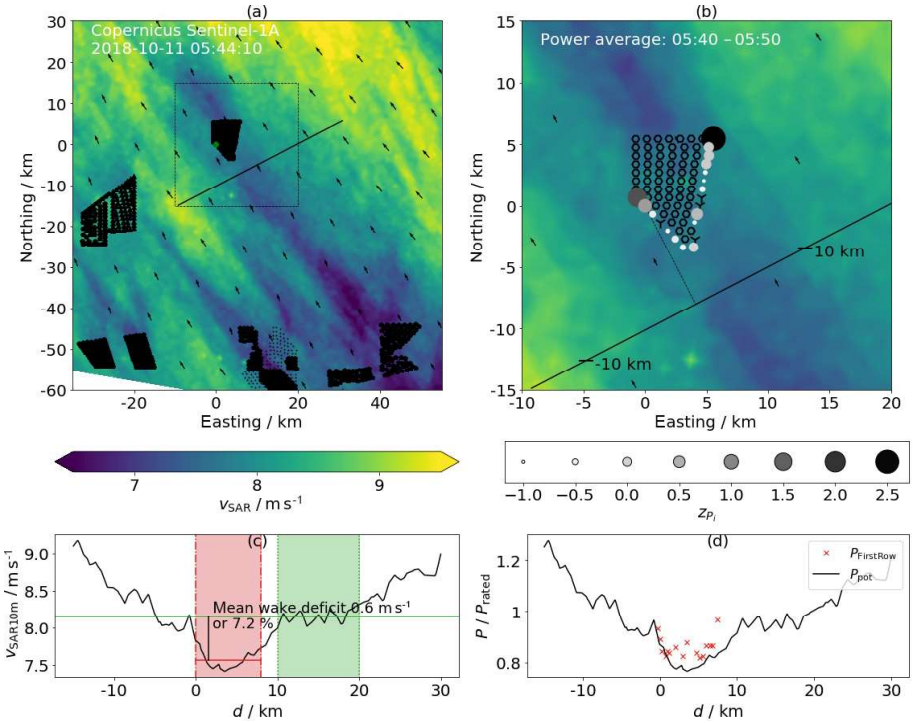

Figure 9. Sentinel-1A Ocean Wind Field (Copernicus Sentinel data (2018)); measurement taken 11 October 2018 05:44:10 UTC. We show power data of the upstream turbines in the interval 05:40–05:50 UTC, as in Fig. 5; positions of downstream turbines are marked (hexagon). In **(d)** we added an offset of 2.0 m s^{-1} to the SAR wind speeds on the virtual wake cut 9000 m upstream of GT58 before we transferred them to hub height and calculated the potential power. Numbers of considered upstream turbines to calculate the z score are 8, 15, 22, 29, 36, 43, 50, 68, 72, 80, 79, 76, 73, 64, 58, and 51.

tion of wake and free stream in the lidar and SAR wind measurements agreeing with the findings of Platis et al. (2018), who present a wake situation with a high wind speed gradient at one side of the cluster wake. In the BorWin case this edge of the wake continues in a separation of the wind farm turbines' power production (Figs. 5–7). In the DolWin2 case we could argue whether the higher power of the outer turbines (Fig. 9b) result from flow effects at the farm corners leading to higher turbine efficiencies as found by Barthelmie and Jensen (2010) but the comparison of the potential power in the inflow with the turbine power (Fig. 9d) reveals a good agreement, suggesting that at least most of the effect originates in the wake-affected inflow conditions with the highest deficit reducing the power of the central turbines, while the outer turbines profit from higher wind speeds at the sides of the wake.

Wakes are expected to exist far downstream in stable stratifications but to recover much earlier in the unstable case. Platis et al. (2018) report about 41 measurement flights (24× stable, 12× unstable, 5× neutral stratification) and find evidence for cluster wakes in stable boundary layers 55 km downstream, while the furthest evidence in an unstable case is found 10 km downstream. In our lidar measurements we find the most pronounced cluster wakes in stable situations supporting these findings. But we have evidence for far-reaching wakes in neutral and weakly unstable conditions, too. All lidar measurements we present in this work were measured in stable situations but the SAR image of the DolWin2 case (Fig. 9) was taken earlier the same day in a shallow, weakly unstable boundary layer with cluster wakes appearing downstream of many clusters. Vertical momentum transport was possible in lower heights but was hindered by an inversion appearing at approximately 200 to 300 m. The rotor area of the GT I turbines extends up to 150 m height. The DolWin2 wake reaches 55 km downstream until it hits the wind farm GT I where the power production of the upstream-row turbines follows the potential power calculated from the inflow SAR wind. This finding proves the existence of long-reaching cluster wakes and their influence on power production of far downstream wind farms even in cases with weakly unstable stratification. In future work we plan to publish an analysis of the whole data set of the, at the time of writing, still ongoing lidar measurement campaign focusing on wakes in unstable conditions. Nevertheless, the DolWin2 case highlights the necessity to carefully characterize the boundary layer for stability analysis, since the unstable stratified layer in the boundary layer could be thin and limited by an inversion just above temperature measurement height and still within the rotor area.

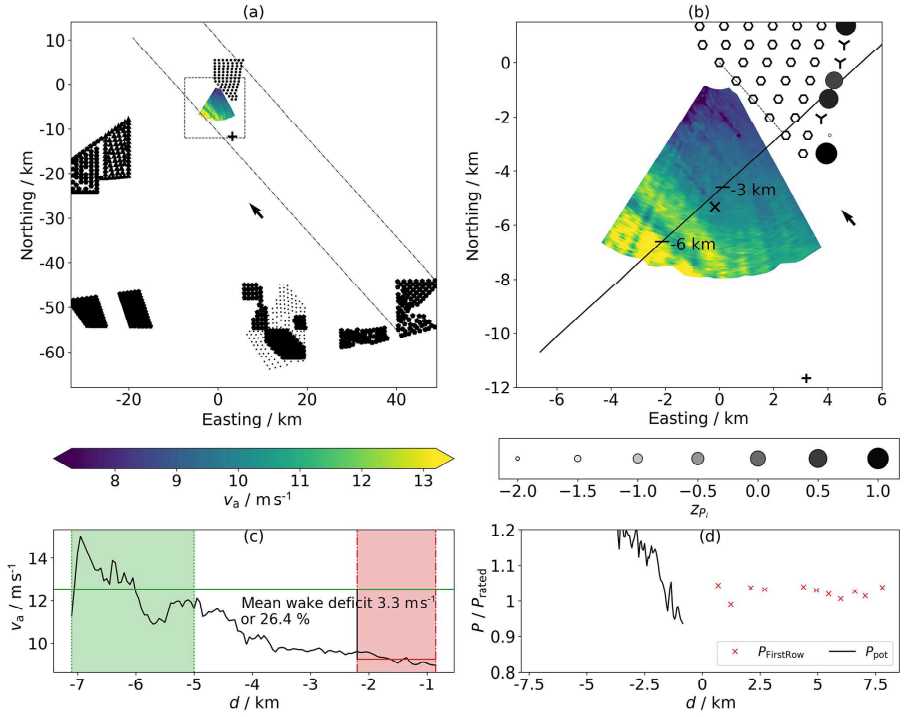

Figure 10. Lidar measurement (scenario A) of the wake of the DolWin2 cluster on 11 October 2018 17:16–17:20 UTC; power data of upstream turbines 17:10–17:20 UTC, as in Fig. 6. Downstream turbine positions marked (hexagon). Turbine numbers to calculate the z score are 8, 15, 22, 29, 36, 43, 50, 68, 72, 78, and 80. Additionally, we marked the converter platform BorWin gamma (+).

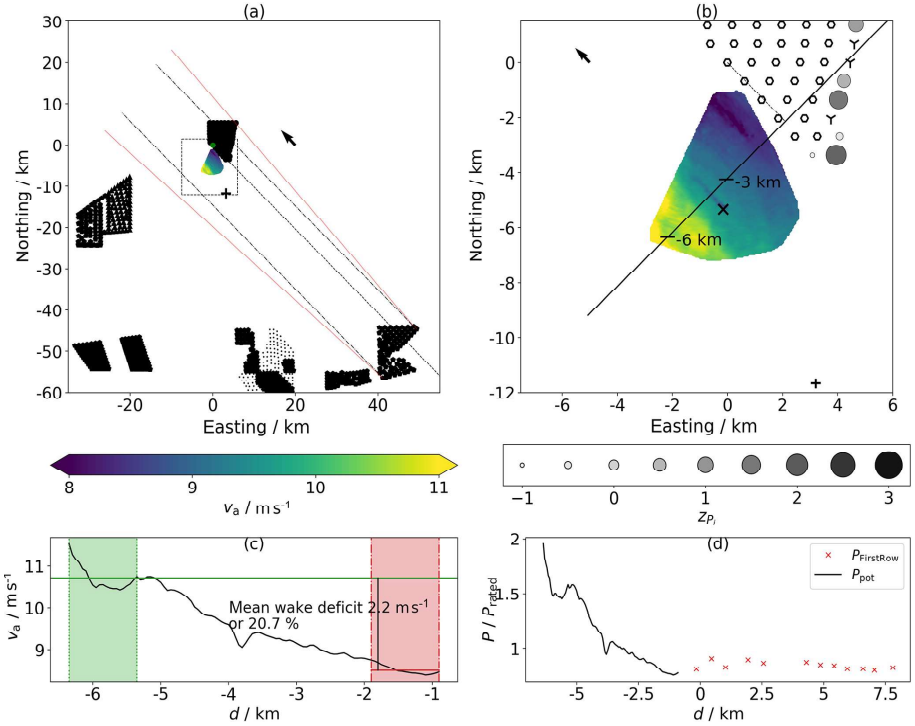

Figure 11. Wake of the DolWin2 cluster on 11 October 2018 as in Fig. 6 but averaged over 16 consecutive lidar scans (scan scenario A) in a period of 162 min (15:44–18:26 UTC); power data of upstream turbines averaged over 170 min (15:40–18:30 UTC); downstream turbines marked (hexagon). Turbine numbers to calculate the z score are 8, 15, 22, 29, 36, 43, 50, 68, 72, 78, 80, and 79.

In addition to the influence of a cluster wake on the wind farm GT I, we still observe inner-farm wake effects (Figs. 5 and 6) with decreasing power production downstream. Cluster wake and wind turbine wakes in the farm overlap. This supports the assumption of the cluster wake being a region of reduced wind speeds with no special characteristics of the original single turbine wakes remaining. We do not perform turbulence analysis comparing cluster wake turbulence to free-flow turbulence in this study. Platis et al. (2018) report a slender wake of increased turbulent kinetic energy (TKE) originating in one corner of the cluster. It was aligned with a stronger horizontal wind speed gradient at the border of the wake. The TKE was reduced in the wake deficit due to the lower wind speeds.

The influence of cluster wakes on the current power production of downstream wind farms could not easily be related to their influence on the annual energy production (AEP). To achieve this, a detailed assessment of the total influence during at least 1 year has to be conducted using, for example, validated wind farm parameterizations in mesoscale models. The local distribution of wind speed, direction and atmospheric stability has to be considered as well as farm and cluster geometries.

In many wake cases the wind speed in the wake deficit still exceeds rated wind speed of the downstream turbines without an effect on their power production. If the upstream cluster's turbines operate in wind speeds above rated speed, their thrust coefficient, c_T, decreases additionally, resulting in reduced wake deficits. We expect the total influence of cluster wakes on AEP to be smaller than wake effects from neighbouring wind farms (see Nygaard and Hansen, 2016) due to cluster wake recovery and a smaller wake-influenced wind direction sector. Our findings do not question wind energy utilization of any kind. Nevertheless, a detailed assessment of the influence of cluster wakes on AEP of downstream wind farms during their whole operational life time considering all planned wind energy activities in the region should be conducted in the future. This can improve power production, offshore resource assessment and consequently reduce the uncertainties in financing large offshore wind projects especially in regions with a high level of (planned) wind energy utilization. Therefore, further research is necessary to validate wind farm parameterizations in mesoscale weather models with appropriate wake, power and atmospheric measurements. Especially the influence of atmospheric stability on cluster wake recovery has to be investigated.

Aside from influence on power, the effect on additional wind turbine loads can be relevant. We did not perform analysis of the turbulence in the wake in this study or load simulations on wind turbines affected by far cluster wakes. Since we find sharp edges between wake flow and free stream continuing in the wind farm's power production (Fig. 6), future research should analyse turbine loads dependent on the cluster wake dynamics, e.g. when a turbine on the wake border has to speed up and slow down fast caused by cluster wake dynamics.

4.2 Cluster wake characteristics

Wind turbines are sensitive to the wind conditions over a wide range of heights defined by the swept rotor area. Therefore, the investigation of cluster wakes should cover the whole vertical wind profile at least from lower to upper tip height. Satellite SAR measurements at the sea surface are typically transferred to 10 m height. Platis et al. (2018) investigates cluster wakes at hub height with a research aircraft in stable stratification, and Siedersleben et al. (2018b) additionally presents measurements in five different height levels (60, 90, 120, 150, 220 m) from the same flight, revealing wake deficits in all regarded levels. This highlights a vertical expansion of the wake far above the rotor area (upper tip height: 150 m). We find evidence for cluster wake effects in SAR images (roughness measurement on the sea surface, interpolation to 10 m a.s.l. – above sea level), lidar measurements ($\approx$ 24.6 m a.m.s.l., 67.0 m below hub height and 9.0 m below lower blade tip height) and from the turbines' power production (rotor swept area spans from 33.6 m to 149.6 m a.m.s.l.). A quantitative comparison of the measured wake strengths is not possible with our data due to the very different type of the measurements. Nevertheless we obtain evidence for wake effects in the boundary layer from the sea surface to the upper tip height 24 and 55 km downstream, agreeing with the observed vertical wake extension closer to the generating cluster presented by Siedersleben et al. (2018b). For a future campaign we suggest the assessment of the development of the atmospheric boundary layer from the inflow through a cluster and in the cluster wake by means of, for example, lidar profilers, lidar range height indicator scans (RHI) or flight measurements for a better understanding of cluster wake development and recovery.

All previous investigations of cluster wakes with satellite SAR suffer from the fact that just one snapshot of the wake is available for a given situation and no wake dynamics or their steadiness could be analysed. Nygaard and Newcombe (2018) investigate a cluster wake at hub height up to 17 km downstream of a wind farm with dual Doppler radar from the coast and present a 1 h average wake field. The aircraft measurements performed by Platis et al. (2018) cover the whole area of the wake along the flight path taking several hours, indicating a constant behaviour of the wake. We find steady wake conditions in both presented examples for more then 2.5 h in the lidar data supported by the corresponding power data. This proves the existence of steady wake effects with a steady influence on the downstream wind farm for constant wind directions. Wake cases with changing wind directions are much harder to analyse since the wake just shortly influences the farm and will probably not even be detectable in wind measurements.

We did not find any evidence for single wind turbine wakes in the lidar inflow measurements of GT I. This is supported by the results by Nygaard and Newcombe (2018), who present dual Doppler radar cross stream flow cuts through a cluster wake at different downstream distances with disappearing signatures of the single turbines from 6 km downstream (unknown stability).

The shapes of the wakes we find could give further hints on the wake recovery process. While shorter wakes (i.e. from the BorWin cluster, Fig. 5) are as wide as the generating cluster, wakes originating further away often appear narrower in the lidar measurements as if they already recovered from the sides or if the whole wake widened with a resulting decrease in maximum wake deficit. This is supported by the shapes of the wakes seen in the SAR wind data in Fig. 9b where the highest wake deficits are narrower further downstream. A detailed analysis of this effect is difficult due to changes in the mesoscale wind field and wakes of neighbouring clusters overlapping with the cluster wake.

The width of the transition region between free flow and wake seems to (at least partly) depend on the downstream position of the wake. In the BorWin wake we sometimes find high wind speed gradients at the wake's border about 20 km downstream (Fig. 6), while in the DolWin wake 50 km downstream the transition region was several kilometres wide (Fig. 10).

The longevity of wakes in stable conditions is further supported by the investigation of two different converter platform wakes in our lidar measurements ranging at least 9 km downstream in one case (Fig. 10). Platform wakes have been observed before, e.g. Chunchuzov et al. (2000) reported a more than 60 km long wake of a 164 m tall offshore platform in very stable atmospheric conditions analysed with satellite SAR measurements. We did not investigate the effect of the wakes of wind farm converter platforms on the power of neighbouring or distant wind turbines but expect it to be fairly small compared to a wind turbine wake due to the lower heights and smaller cross sections of the platforms.

4.3 Cluster wake monitoring

Due to the large areas the cluster wakes take up, their investigation was mainly based on long-ranging remote-sensing techniques. Satellite SAR covers large areas and has been widely used to analyse cluster wakes (Hasager et al., 2015). Our analysis adds the potential power as a computed local quantity to the SAR analysis (Fig. 5d), confirming the wake shape acquired by SAR with turbine power data. This is another hint for the ability of satellite SAR to resolve flow structures, agreeing with the findings of Schneemann et al. (2015), who compared structures in concurrent SAR and lidar measurements indicating the general ability of SAR to resolve flow structures with the size of a few hundred metres.

Cluster wakes have not been measured with long-range lidar. With an achievable maximum range of 10 km with compact devices, lidar seemed not to be appropriate to measure far cluster wakes behind a wind farm. We used lidar to measure incoming far cluster wakes. As opposed to SAR, lidar allows for continuous measurements with scan repetition times in the order of a few minutes (2.5 and 10 min here). In some cases the lidar results are clear (e.g. Fig. 6) but in other cases it is difficult to interpret whether the wind field is influenced by a wake or not. Here, satellite SAR, when available, proves very useful to interpret wind monitoring by lidar offering the possibility to regard the lidar wind field in a wider context (e.g. the DolWin2 case, Sect. 3.2). Nevertheless, absolute wind speed measurements by satellite SAR are comparably imprecise. For the comparison of the shapes of the potential power in the inflow with the turbines' power, we had to correct individual offsets in the SAR wind speeds within the given measurement accuracy. Schneemann et al. (2015) had to correct for an offset in SAR winds, comparing it with lidar, as well. This inaccuracy could be possibly reduced by a SAR analysis tuned to the special case. We did not perform SAR wind calculations ourselves but used already processed wind data.

The analysis of SCADA data on power losses due to cluster wakes without additional flow information from remote sensing is difficult since obvious gradients in wind farm power (Fig. 6) due to cluster wakes are rare and not exactly stationary (e.g. washed out transition region in averaged lidar wind field, Fig. 7b). In the DolWin2 case (Fig. 9) it is hardly possible to judge the contributions of wake effects and effect of higher turbine efficiency at the farm corners (Barthelmie and Jensen, 2010) on the higher power of the turbines at the eastern and western corners of the farm.

For future research on cluster wakes and their influence on power generation, we propose a combination of different measurement techniques complementing with their advantages, namely satellite SAR, long-range lidar and flight measurements (aircrafts and drones). Doppler radar and non-compact lidar systems offering ranges larger than 15 km are available but have not been deployed in offshore wind farms so far due to high costs and technical hurdles in the deployment, orientation and operation of the container-size systems on offshore structures.

Another important aspect of measurements from offshore platforms like transition pieces of offshore wind turbines to be considered is platform movement and the resulting errors in measurement locations. We found platform tilts of up to 0.1° due to turbine thrust depending on wind speed and direction using the method of sea surface levelling (Rott et al., 2017). This value might be even higher for turbines on a commonly used monopile foundation compared to the tripod foundation used in GT I. With increasing measurement ranges, the location error in the measurements grows further.

5 Conclusions

This paper investigates the question of whether offshore cluster wakes have an influence on power generation of far downstream wind farms considering atmospheric stability. Therefore we analysed two different cases of 24 and 55 km long cluster wakes approaching the 400 MW offshore wind farm Global Tech I (GT I) by means of satellite SAR measurements, lidar wind monitoring and analysis of atmospheric stability and GT I power production.

Long-range Doppler lidar supported by satellite SAR proves to be a good combination for cluster wake measurements with the lidar providing accurate wind speed monitoring over long periods and SAR contributing with large-area wind fields for the overall picture.

We find that long-distance wake effects of a wind farm cluster exist at least 55 km downstream in stable and weakly unstable stratification. They persist for more than 2.5 h. During this measurement period the average wake deficits are $2.3\,\mathrm{m\,s^{-1}}$ or 25 % approximately 24 km downstream and $2.2\,\mathrm{m\,s^{-1}}$ or 21 % approximately 55 km downstream. Single lidar scans (2.5 min duration) reveal stronger wake deficits of up to $3.9\,\mathrm{m\,s^{-1}}$ or 41 % approximately 24 km downstream.

Clear transition regions like edges in the wind separate wake and free flow 24 km downstream and continue in the affected wind farm, splitting it into regions of higher power in undisturbed flow and reduced power in the wake deficit. Free-flow turbines produce more then two standard deviations, σ_P, more than the average of the upstream turbines.

This contribution proves the existence of steady power reductions in a far downstream wind farm caused by cluster wakes. We encourage further investigations on far-reaching wake shadowing effects for optimized areal planning at sea and reduced uncertainties in offshore wind power resource assessment.

Data availability. Lidar data and meteorological data are published (Schneemann et al., 2019). GT I SCADA data are confidential and therefore not available to the public. SAR wind data are available from https://scihub.copernicus.eu/ (last access: 13 December 2019; Scihub, 2019). Hourly power data for several wind farms are available from https://www.energy-charts.de/ (last access: 19 December 2019; Fraunhofer ISE, 2019). The New European Wind Atlas is published at https://map.neweuropeanwindatlas.eu/ (last access: 19 December 2019; NEWA, 2019). The OSTIA data set can be obtained from http://marine.copernicus.eu/ (last access: 13 December 2019; Copernicus marine service, 2019) and radiosonde soundings are available at
http://www.meteociel.fr/ (last access: 13 December 2019; meteociel.fr, 2019) or
http://weather.uwyo.edu (last access: 13 December 2019; University of Wyoming, 2019).

Appendix A: Calculation of virtual potential temperatures

We derived the virtual potential temperature used in Sect. 2.4 from the available measurements on the TP. We adapted the following methodology mainly from Etling (2008). We need the following:

- $R_\mathrm{d} = 287\,\mathrm{J\,K^{-1}\,kg^{-1}}$ (specific gas constant of dry air);
- $R_\mathrm{v} = 461\,\mathrm{J\,K^{-1}\,kg^{-1}}$ (specific gas constant of water vapour);
- $\epsilon = \frac{R_\mathrm{d}}{R_\mathrm{v}} = 0.622$ (ratio between the specific gas constants for dry air R_d and water vapour R_v);
- $\kappa_\mathrm{P} = 0.286$ (Poisson constant in dry air).

The saturation vapour pressure in pascals (Pa) dependent on the temperature in kelvin (K) follows from the Magnus equation,

$$e_\mathrm{s}(T) = 100.0 \cdot 6.1 \cdot 10^{\left(\frac{7.45\cdot(T-273.15)}{T-38.15}\right)}. \tag{A1}$$

The partial pressure of water vapour in the air dependant on the relative humidity RH reads as

$$e = \mathrm{RH} \cdot e_\mathrm{s}/100.0, \tag{A2}$$

while the mixing ratio is

$$r_\mathrm{v} = \epsilon \cdot \left(\frac{e}{p-e}\right). \tag{A3}$$

With the specific humidity

$$q = \frac{r_\mathrm{v}}{1+r_\mathrm{v}} \tag{A4}$$

and the potential temperature

$$\Theta = T\left(\frac{100\,000\,\mathrm{Pa}}{p}\right)^{\kappa_\mathrm{P}}, \tag{A5}$$

we approximate the virtual potential temperature as

$$\Theta_\mathrm{v} = \Theta \cdot (1.0 + 0.61 \cdot q). \tag{A6}$$

While the virtual potential temperature at the TP, $\Theta_{\mathrm{v,TP}}$, could be derived directly from the available measurements, we assume the relative humidity and the air temperature directly above the sea to be $\mathrm{RH}_0 = 100\,\%$ and $T_0 = T_\mathrm{SST}$, respectively, to derive the virtual potential temperature at sea level, $\Theta_{\mathrm{v,SST}}$. Furthermore we calculate the air pressure at sea level as

$$p_0 = p_\mathrm{TP} \cdot \left(\frac{T_\mathrm{SST} - \gamma \cdot z_\mathrm{TP}}{T_\mathrm{SST}}\right)^{\frac{-g}{\gamma R_\mathrm{d}}}, \tag{A7}$$

assuming a polytropic atmosphere and using the air temperature gradient

$$\gamma = \frac{T_\mathrm{SST} - T_\mathrm{TP}}{z_\mathrm{TP}}. \tag{A8}$$

Author contributions. JS conducted and supervised the measurement campaign, designed the research, performed the data analysis, made the figures, and planned and wrote the paper. AR and MK contributed to the research with intensive discussions and added to the paper with conceptual discussions and internal review. MD advised on the meteorological parts, participated in the conception of the paper and did an internal review. GS performed parts of the stability analysis and intensively reviewed the article.

Competing interests. The authors declare that they have no conflict of interest.

Acknowledgements. We acknowledge the wind farm operator Global Tech I Offshore Wind GmbH for providing SCADA data and their support of the work. Furthermore, we thank the European Space Agency (ESA) for making the Sentinel-1 data of the Copernicus programme available. Thanks to the Met Office for making the OSTIA data set available. We acknowledge the NEWA consortium for providing access to the New European Wind Atlas. Special thanks to Stephan Voß for his work on the measurement campaign and the picture from Fig. 3.

Financial support. The lidar measurements and parts of the work have been supported by the German Federal Ministry for Economic Affairs and Energy on the basis of a decision by the German Bundestag (OWP Control, grant no. 0324131A).

Review statement. This paper was edited by Rebecca Barthelmie and reviewed by Nicolai Gayle Nygaard and one anonymous referee.

References

Abkar, M. and Porté-Agel, F.: Influence of atmospheric stability on wind-turbine wakes: A large-eddy simulation study, Phys. Fluids, 27, 035104, https://doi.org/10.1063/1.4913695, 2015.

Aitken, M. L., Banta, R. M., Pichugina, Y. L., and Lundquist, J. K.: Quantifying Wind Turbine Wake Characteristics from Scanning Remote Sensor Data, J. Atmos. Ocean. Tech., 31, 765–787, https://doi.org/10.1175/JTECH-D-13-00104.1, 2014.

Barthelmie, R. J. and Jensen, L. E.: Evaluation of wind farm efficiency and wind turbine wakes at the Nysted offshore wind farm, Wind Energy, 13, 573–586, https://doi.org/10.1002/we.408, 2010.

Beck, H. and Kühn, M.: Dynamic Data Filtering of Long-Range Doppler LiDAR Wind Speed Measurements, Remote Sens., 9, 561, https://doi.org/10.3390/rs9060561, 2017.

Beck, H. and Kühn, M.: Temporal Up-Sampling of Planar Long-Range Doppler LiDAR Wind Speed Measurements Using Space-Time Conversion, Remote Sens., 11, 867, https://doi.org/10.3390/rs11070867, 2019.

Bodini, N., Zardi, D., and Lundquist, J. K.: Three-dimensional structure of wind turbine wakes as measured by scanning lidar, Atmos. Meas. Tech., 10, 2881–2896, https://doi.org/10.5194/amt-10-2881-2017, 2017.

Christiansen, M. B. and Hasager, C. B.: Wake effects of large offshore wind farms identified from satellite SAR, Remote Sens. Environ., 98, 251–268, https://doi.org/10.1016/j.rse.2005.07.009, 2005.

Chunchuzov, I., Vachon, P., and Li, X.: Analysis and Modeling of Atmospheric Gravity Waves Observed in RADARSAT SAR Images, Remote Sens. Environ., 74, 343–361, https://doi.org/10.1016/S0034-4257(00)00076-6, 2000.

Churchfield, M. J., Lee, S., Michalakes, J., and Moriarty, P. J.: A numerical study of the effects of atmospheric and wake turbulence on wind turbine dynamics, J. Turbulence, 13, N14, https://doi.org/10.1080/14685248.2012.668191, 2012.

Copernicus marine service: Copernicus Marine environment monitoring service, available at: http://marine.copernicus.eu/, last access: 13 December 2019.

Donlon, C. J., Martin, M., Stark, J., Roberts-Jones, J., Fiedler, E., and Wimmer, W.: The Operational Sea Surface Temperature and Sea Ice Analysis (OSTIA) system, Remote Sens. Environ., 116, 140–158, https://doi.org/10.1016/j.rse.2010.10.017, 2012.

Dörenkämper, M., Optis, M., Monahan, A., and Steinfeld, G.: On the Offshore Advection of Boundary-Layer Structures and the Influence on Offshore Wind Conditions, Bound.-Lay. Meteorol., 155, 459–482, https://doi.org/10.1007/s10546-015-0008-x, 2015a.

Dörenkämper, M., Witha, B., Steinfeld, G., Heinemann, D., and Kühn, M.: The impact of stable atmospheric boundary layers on wind-turbine wakes within offshore wind farms, J. Wind Eng. Indust. Aerodynam., 144, 146–153, https://doi.org/10.1016/j.jweia.2014.12.011, 2015b.

Emeis, S.: A simple analytical wind park model considering atmospheric stability, Wind Energy, 13, 459–469, https://doi.org/10.1002/we.367, 2009.

Emeis, S.: Wind Energy Meteorology, Springer International Publishing, 2nd Edn, Springer International Publishing AG, part of Springer Nature 2018, https://doi.org/10.1007/978-3-319-72859-9, 2018.

EnBW: EnBW Hohe See and Albatros wind farms, The construction diary for Hohe available at: https://www.enbw.com/renewable-energy/wind-energy/our-offshore-wind-farms/hohe-see/construction-diary.html, (last access: 18 June 2019.

ESA: Level 2 OCN Ocean Wind Field (OWI) Component, available at: https://sentinel.esa.int/web/sentinel/ocean-wind-field-component, last access: 19 June 2019.

Etling, D.: Theoretische Meteorologie, 3rd Edn., Springer, Berlin, Heidelberg, https://doi.org/10.1007/978-3-662-10430-9, 2008.

Fitch, A. C., Olson, J. B., Lundquist, J. K., Dudhia, J., Gupta, A. K., Michalakes, J., and Barstad, I.: Local and Mesoscale Impacts of Wind Farms as Parameterized in a Mesoscale NWP Model, Mon. Weather Rev., 140, 3017–3038, https://doi.org/10.1175/mwr-d-11-00352.1, 2012.

Fraunhofer ISE: Energy Charts, available at: https://www.energy-charts.de/, last access: 19 June 2019.

Fuertes, F. C., Markfort, C., and Porté-Agel, F.: Wind Turbine Wake Characterization with Nacelle-Mounted Wind Lidars for Analytical Wake Model Validation, Remote Sens., 10, 668, https://doi.org/10.3390/rs10050668, 2018.

Grachev, A. A. and Fairall, C. W.: Dependence of the Monin–Obukhov Stability Parameter on the Bulk Richardson Number over the Ocean, J. Appl. Meteorol., 36, 406–414, https://doi.org/10.1175/1520-0450(1997)036<0406:dotmos>2.0.co;2, 1997.

Hansen, K. S., Barthelmie, R. J., Jensen, L. E., and Sommer, A.: The impact of turbulence intensity and atmospheric stability on power deficits due to wind turbine wakes at Horns Rev wind farm, Wind Energy, 15, 183–196, https://doi.org/10.1002/we.512, 2011.

Hasager, C., Vincent, P., Badger, J., Badger, M., Bella, A. D., Peña, A., Husson, R., and Volker, P.: Using Satellite SAR to Characterize the Wind Flow around Offshore Wind Farms, Energies, 8, 5413–5439, https://doi.org/10.3390/en8065413, 2015.

Hirth, B. D., Schroeder, J. L., Gunter, W. S., and Guynes, J. G.: Coupling Doppler radar-derived wind maps with operational turbine data to document wind farm complex flows, Wind Energy, 18, 529–540, https://doi.org/10.1002/we.1701, 2014.

Lee, S., Vorobieff, P., and Poroseva, S.: Interaction of Wind Turbine Wakes under Various Atmospheric Conditions, Energies, 11, 1442, https://doi.org/10.3390/en11061442, 2018.

Li, X. and Lehner, S.: Observation of TerraSAR-X for Studies on Offshore Wind Turbine Wake in Near and Far Fields, IEEE J. Select. Top. Appl. Earth Obs. Remote Sens., 6, 1757–1768, https://doi.org/10.1109/jstars.2013.2263577, 2013.

Lignarolo, L. E., Mehta, D., Stevens, R. J., Yilmaz, A. E., van Kuik, G., Andersen, S. J., Meneveau, C., Ferreira, C. J., Ragni, D., Meyers, J., van Bussel, G. J., and Holierhoek, J.: Validation of four LES and a vortex model against stereo-PIV measurements in the near wake of an actuator disc and a wind turbine, Renewable Energy, 94, 510–523, https://doi.org/10.1016/j.renene.2016.03.070, 2016.

Lundquist, J. K., DuVivier, K. K., Kaffine, D., and Tomaszewski, J. M.: Costs and consequences of wind turbine wake effects arising from uncoordinated wind energy development, Nat. Energy, 4, 26–34, https://doi.org/10.1038/s41560-018-0281-2, 2019.

Mackensen, R.: Windenergie Report Deutschland 2018, available at: http://windmonitor.iee.fraunhofer.de/opencms/export/sites/windmonitor/img/Windmonitor-2018/WERD_2018.pdf, last access: 5 July 2019.

Merkur Offshore: Sea Change: GE Installs The Last Turbine At One Of Germany's Largest Offshore Wind Farms, available at: https://www.merkur-offshore.com/progress/ (last access: 19 June 2019), 2018.

meteociel.fr: Observation, Prévisions, Modèles, En temps réel, available at: https://www.meteociel.fr/, last access: 13 December 2019.

Mouche, A.: Sentinel-1 Ocean Wind Fields (OWI) Algorithm Definition, Tech. Rep. CLS-DAR-NT-10-167 S1-TN-CLS-52-904, CLS/ESA, available at: https://sentinel.esa.int/documents/247904/349449/S-1_L2_OWI_Detailed_Algorithm_Definition.pdf (last access: 22 February 2019), 2011.

NEWA: New European Wind Atlas, available at: https://map.neweuropeanwindatlas.eu/, last access: 27 June 2019.

Nygaard, N. G.: Wakes in very large wind farms and the effect of neighbouring wind farms, J. Phys.: Conf. Ser., 524, 012162, https://doi.org/10.1088/1742-6596/524/1/012162, 2014.

Nygaard, N. G. and Hansen, S. D.: Wake effects between two neighbouring wind farms, J. Phys.: Conf. Ser., 753, 032020, https://doi.org/10.1088/1742-6596/753/3/032020, 2016.

Nygaard, N. G. and Newcombe, A. C.: Wake behind an offshore wind farm observed with dual-Doppler radars, J. Phys.: Conf. Ser., 1037, 072008, https://doi.org/10.1088/1742-6596/1037/7/072008, 2018.

Orsted: Borkum Riffgrund 2, available at: https://orsted.de/offshore-windenergie/unsere-offshore-windparks-nordsee/offshore-windpark-borkum-riffgrund-2 (last access: 19 June 2019), 2018.

Petrofac: BorWin gamma platform topside touches down in the German North Sea, available at: https://www.petrofac.com/en-gb/media/news/borwin-gamma-platform-topside-touches-down-in-the-german-north-sea/ (last access: 7 June 2019), 2018.

Platis, A., Siedersleben, S. K., Bange, J., Lampert, A., Bärfuss, K., Hankers, R., Cañadillas, B., Foreman, R., Schulz-Stellenfleth, J., Djath, B., Neumann, T., and Emeis, S.: First in situ evidence of wakes in the far field behind offshore wind farms, Scient. Rep., 8, 2163, https://doi.org/10.1038/s41598-018-20389-y, 2018.

Pryor, S. C., Barthelmie, R. J., and Shepherd, T. J.: The Influence of Real-World Wind Turbine Deployments on Local to Mesoscale Climate, J. Geophys. Res.-Atmos., 123, 5804–5826, https://doi.org/10.1029/2017jd028114, 2018a.

Pryor, S. C., Shepherd, T. J., and Barthelmie, R. J.: Interannual variability of wind climates and wind turbine annual energy production, Wind Energ. Sci., 3, 651–665, https://doi.org/10.5194/wes-3-651-2018, 2018b.

Rodrigo, J. S., Cantero, E., García, B., Borbón, F., Irigoyen, U., Lozano, S., Fernande, P. M., and Chávez, R. A.: Atmospheric stability assessment for the characterization of offshore wind conditions, J. Phys.: Conf. Ser., 625, 012044, https://doi.org/10.1088/1742-6596/625/1/012044, 2015.

Rott, A., Schneemann, J., Trabucchi, D., Trujillo, J., and Kühn, M.: Accurate deployment of long range scanning lidar on offshore platforms by means of sea surface leveling, in: Poster presentation, NAWEA Windtech, available at: http://windtechconferences.org/wp-content/uploads/2018/01/Windtech2017_AnRott-Poster.pdf (last access: 5 July 2019), 2017.

Schmidt, J. and Stoevesandt, B.: The impact of wake models on wind farm layout optimization, J. Phys.: Conf. Ser., 625, 012040, https://doi.org/10.1088/1742-6596/625/1/012040, 2015.

Schneemann, J., Hieronimus, J., Jacobsen, S., Lehner, S., and Kühn, M.: Offshore wind farm flow measured by complementary remote sensing techniques: radar satellite TerraSAR-X and lidar windscanners, J. Phys.: Conf. Ser., 625, 012015, https://doi.org/10.1088/1742-6596/625/1/012015, 2015.

Schneemann, J., Voß, S., Rott, A., and Kühn, M.: Doppler wind lidar plan position indicator scans and atmospheric measurements at the offshore wind farm "Global Tech I", PANGAEA – Data Publisher for Earth & Environmental Science, https://doi.org/10.1594/PANGAEA.909721, 2019.

Scihub: ESA, Copernicus Open Access Hub, available at: https://scihub.copernicus.eu/, last access: 13 December 2019.

Siedersleben, S. K., Lundquist, J. K., Platis, A., Bange, J., Bärfuss, K., Lampert, A., Cañadillas, B., Neumann, T., and Emeis, S.: Micrometeorological impacts of offshore wind farms as seen in observations and simulations, Environ. Res. Lett., 13, 124012, https://doi.org/10.1088/1748-9326/aaea0b, 2018a.

Siedersleben, S. K., Platis, A., Lundquist, J. K., Lampert, A., Bärfuss, K., Cañadillas, B., Djath, B., Schulz-Stellenfleth, J., Bange, J., Neumann, T., and Emeis, S.: Evaluation of a Wind Farm Parametrization for Mesoscale Atmospheric Flow Models with Aircraft Measurements, Meteorol. Z., 27, 401–415, https://doi.org/10.1127/metz/2018/0900, 2018b.

Sorbjan, Z. and Grachev, A. A.: An Evaluation of the Flux-Gradient Relationship in the Stable Boundary Layer, Bound.-Lay. Meteorol., 135, 385–405, https://doi.org/10.1007/s10546-010-9482-3, 2010.

Trabucchi, D., Trujillo, J.-J., and Kühn, M.: Nacelle-based Lidar Measurements for the Calibration of a Wake Model at Different Offshore Operating Conditions, Energy Procedia, 137, 77–88, https://doi.org/10.1016/j.egypro.2017.10.335, 2017.

Turner, S., Romero, D., Zhang, P., Amon, C., and Chan, T.: A new mathematical programming approach to optimize wind farm layouts, Renew. Energy, 63, 674–680, https://doi.org/10.1016/j.renene.2013.10.023, 2014.

University of Wyoming: Wyoming weather web, available at: http://weather.uwyo.edu/, last access: 13 December 2019.

Vincent, P., Bourbigot, M., Johnsen, H., and Piantanida, R.: Sentinel-1 Product Specification, Tech. Rep. S1-RS-MDA-52-7441, ESA, available at: https://sentinel.esa.int/web/sentinel/user-guides/sentinel-1-sar/document-library/-/asset_publisher/1dO7RF5fJMbd/content/sentinel-1-product-specification, last access: 13 December 2019.

Volker, P. J. H., Badger, J., Hahmann, A. N., and Ott, S.: The Explicit Wake Parametrisation V1.0: a wind farm parametrisation in the mesoscale model WRF, Geosci. Model Dev., 8, 3715–3731, https://doi.org/10.5194/gmd-8-3715-2015, 2015.

Vollmer, L., Steinfeld, G., Heinemann, D., and Kühn, M.: Estimating the wake deflection downstream of a wind turbine in different atmospheric stabilities: an LES study, Wind Energ. Sci., 1, 129–141, https://doi.org/10.5194/wes-1-129-2016, 2016.

Witha, B., Hahmann, A., Sīle, T., Dörenkämper, M., Ezber, Y., García-Bustamante, E., González-Rouco, J. F., Leroy, G., and Navarro, J.: WRF model sensitivity studies and specifications for the NEWA mesoscale wind atlas production runs, Technical report, The NEWA consortium, 73 pp., https://doi.org/10.5281/zenodo.2682604, 2019.

Wind Energ. Sci., 7, 1241–1262, 2022
https://doi.org/10.5194/wes-7-1241-2022

eawe european academy of wind energy
Open Access
WIND ENERGY SCIENCE

Offshore wind farm cluster wakes as observed by long-range-scanning wind lidar measurements and mesoscale modeling

Beatriz Cañadillas[1,2], Maximilian Beckenbauer[1], Juan J. Trujillo[2], Martin Dörenkämper[3], Richard Foreman[2], Thomas Neumann[2], and Astrid Lampert[1]

[1]Institute of Flight Guidance, Technische Universität Braunschweig, Braunschweig, Germany
[2]Renewables, UL International GmbH, Oldenburg, Germany
[3]Fraunhofer Institute for Wind Energy Systems, Oldenburg, Germany

Correspondence: Beatriz Cañadillas [redacted]@tu-braunschweig.de, [redacted]@ul.com)

Received: 21 December 2021 – Discussion started: 18 January 2022
Revised: 25 May 2022 – Accepted: 2 June 2022 – Published: 20 June 2022

Abstract. As part of the ongoing X-Wakes research project, a 5-month wake-measurement campaign was conducted using a scanning lidar installed amongst a cluster of offshore wind farms in the German Bight. The main objectives of this study are (1) to demonstrate the performance of such a system and thus quantify cluster wake effects reliably and (2) to obtain experimental data to validate the cluster wake effect simulated by the flow models involved in the project. Due to the lack of free wind flow for the wake flow directions, wind speeds obtained from a mesoscale model (without any wind farm parameterization) for the same time period were used as a reference to estimate the wind speed deficit caused by the wind farm wakes under different wind directions and atmospheric stabilities. For wind farm waked wind directions, the lidar data show that the wind speed is reduced up to 30 % at a wind speed of about 10 m s^{-1}, depending on atmospheric stability and distance to the wind farm. For illustrating the spatial extent of cluster wakes, an airborne dataset obtained during the scanning wind lidar campaign is used and compared with the mesoscale model with wind farm parameterization and the scanning lidar. A comparison with the results of the model with a wind farm parameterization and the scanning lidar data reveals a relatively good agreement in neutral and unstable conditions (within about 2 % for the wind speed), whereas in stable conditions the largest discrepancies between the model and measurements are found. The comparative multi-sensor and model approach proves to be an efficient way to analyze the complex flow situation in a modern offshore wind cluster, where phenomena at different length scales and timescales need to be addressed.

1 Introduction

Offshore wind energy, i.e., the use of wind farms built offshore or on the continental shelf to harvest wind energy for electricity generation, is playing an important role in achieving a low-carbon future of economic prosperity. In 2020, 6.1 GW was commissioned worldwide. The total offshore wind capacity has now passed 35 GW, representing 4.8 % of the total global cumulative wind capacity. In particular, Germany represents a 22 % contribution (7.8 GW) of the total installed power (Lee and Zhao, 2021). In the North Sea, the available offshore area for wind energy is becoming increasingly scarce. In order to contribute to the planned target of 30 GW by 2030 (long-term goal recently approved by the German government) and to make wind energy extraction economically profitable, wind farms need to be installed relatively close to each other. While this may be beneficial in terms of infrastructure sharing, it may also be detrimental to the overall energy extraction due to the influence of the wakes generated by the upstream wind farms.

Therefore, knowledge of the prevailing wind conditions is one of the crucial parts not only in the first phase of a po-

tential offshore wind farm to accurately assess the wind resource, but also during the operation phase of the wind farm. Although numerical simulations and the detailed analysis of experiments in wind tunnels can provide good insight into the actual conditions, high-quality in situ measurements in a real environment are essential.

As the size of offshore wind farms increases and they are grouped into larger arrays, also called clusters, wake effects take on greater importance, not only affecting the surrounding wind conditions but also reducing the efficiency of power generation for downstream wind farms. In the North Sea, for example, the large size of wind farms and their proximity affect not only the performance of single downstream turbines but also that of whole neighboring downstream farms (Cañadillas et al., 2020; Ahsbahs et al., 2020), which may reduce the capacity factor by approximately 20 % or more as suggested by Akhtar et al. (2021). The effect of atmospheric stability on the extension of the wakes behind wind farms has been intensively studied in recent years through a number of analytical and experimental studies (Christiansen and Hasager, 2005; Emeis, 2010, 2018; Djath et al., 2018; Ahsbahs et al., 2018; Nygaard and Newcombe, 2018; Cañadillas et al., 2020; Ahsbahs et al., 2020; Platis et al., 2020), as well as numerical investigations (Patrick et al., 2014; Siedersleben et al., 2018b). For instance, Cañadillas et al. (2020) analyzed data from a series of flights collected within the wakes at several downstream distances of two offshore wind farm clusters located in the North Sea during different atmospheric stability conditions. They found that stable stratification leads to significantly longer wakes with a slower wind speed recovery compared to unstable conditions. Their results reveal that the average wake length (defined as the downstream distance where the wind speed has recovered to 95 % of the free-stream wind speed) under stable conditions exceeds 50 km, while under neutral/unstable conditions, the wake length amounts to around 15 km.

The analysis of wind farm cluster wake interaction is a complex task, as different interacting processes on multiple scales have to be taken into account. On the one hand, these effects depend on climatological and seasonal changes, and on the other hand, the wind farms extend over very large areas, experiencing natural spatial gradients with regard to the wind conditions. This makes it necessary to find new long-term wind speed measurements of the incoming wind, important not only for wind farms already installed but also for future wind farms to be installed in the vicinity of a cluster (Neumann et al., 2020).

Due to the high spatial and temporal resolution, long-range-scanning Doppler wind lidars (also lidar, light detection and ranging) have gained importance in the wind energy industry for a variety of applications, such as wind resource assessment (Neumann et al., 2020), wind turbine and wind farm wake studies (Schneemann et al., 2020), and power performance testing (Rettenmeier et al., 2014; Gómez Arranz and Courtney, 2021). Especially in the offshore sector, traditional masts are associated with a high cost and long approval processes. In contrast, scanning wind lidars are cheaper, very flexible in terms of the scan set-up and the installation (for instance, on a wind turbine transition piece), and easily accessible for system maintenance during the maintenance routines of wind farms. In the past, most studies, using scanning Doppler lidar, have been limited to investigations of the spatial wake characteristics of isolated wind turbines (Wang and Barthelmie, 2015; Bastine et al., 2015; Bingöl et al., 2010; Käsler et al., 2010) or individual wind farms (Smalikho et al., 2013; Aitken et al., 2014; Iungo and Porté-Agel, 2014; Herges et al., 2017; Krishnamurthy et al., 2017; Zhan et al., 2020), such as the velocity deficit, the single wake extent (length and width) of a wake, and wake meandering (Trujillo et al., 2010; Krishnamurthy et al., 2017) under various atmospheric conditions. More recently, lidars have also been used to study the wind speed reduction upstream of a wind farm, the so-called blockage effect (Schneemann et al., 2021). Only a few studies have focused on the effects of cluster wind farm wakes on the wind speed (Schneemann et al., 2020), the value of the scanning lidar measurements for validating wind farm parameterizations in mesoscale models (Goit et al., 2020) or simple wake engineering models used for wind farm optimization and energy yield estimation (e.g., Brower and Robinson, 2012).

Mesoscale models are capable of resolving effects that are relevant on these large scales using wind farm parameterizations developed to account for the wind speed reduction and turbulence increase downstream of wind farms (Fitch et al., 2012; Volker et al., 2015). A validation of simulations with airborne in situ data (Lampert et al., 2020) has been one of the aims of the projects WIPAFF (Wind Park Far Field) and X-Wakes (Interaction of the wake of large offshore wind farms and wind farm clusters with the marine atmospheric boundary layer) (Siedersleben et al., 2018b, a, 2020), and the airborne datasets have been used as reference for the validation of simulations and parameterizations (Akhtar et al., 2021; Larsén and Fischereit, 2021). In this study, in order to determine the wake effects of interacting wind farms, data from different measurement locations and methods are combined with the aim of obtaining a comprehensive picture of the wind situation in the region of an offshore wind farm cluster.

This paper is structured as follows. Section 2 provides an overview of the locations and datasets used, including a thorough description of the scanning lidar set-up, airborne measurements and mesoscale simulations. Section 3.1 presents a direct comparison of the lidar data with high-resolution airborne data in the vicinity of the measurement location; visualization of the aircraft measurements and a mesoscale model data give an example of the spatial extent of wind farm cluster wakes. Section 3.2 shows the influence of upstream wind farms by comparing the scanning lidar data with mesoscale simulations without the wind farm parameterization (to estimate the wind speed deficit) and with consideration of the

wind farm wake (to compare the model output with the in situ scanning data). After a brief discussion of the study, the conclusions are presented in Sects. 4 and 5 respectively, where the potential of the scanning wind lidar for validating wind farm parameterizations in numerical simulations is highlighted.

2 Site and methods

A field campaign using a scanning Doppler lidar was conducted at the western edge of the wind farm Gode Wind 1 in the German Bight (see Fig. 1) for a period of 5 months, from May to September 2020. Additionally, data from the Dornier 128 D-IBUF research aircraft of the Technische Universität (TU) Braunschweig are used for a single flight to extend the range of the available wind speed measurements upstream, around and within the wind farm cluster wakes. Due to the lack of a free wind reference (without any flow disturbance generated by the wind farms), high-resolution mesoscale model data from the Weather Research and Forecasting model (without the wind farm parameterization, hereafter WRF) were used to assess the wind speed deficit due to the presence of wind farms surrounding the lidar measurement location. Moreover, the scanning wind lidar dataset is used to evaluate the WRF model outputs considering wind farm wakes with the wind farm parameterization of Fitch (Fitch et al., 2012), hereafter referred to as the WRF-WF setup.

Starting from the location of the scanning lidar measurements, five different sectors were defined for the subdivision of the measurement data into different wind direction regions. Figure 1 shows a map of the study area in the German Bight with the defined wind direction sectors. The individual regions are labeled R1 to R5.

A detailed description of the measurement methods can be found in the following sections. For the classification into the five different regions according to the wind direction, the actual position of the profile measurements at a distance of 1.5 km west of the scanning lidar device was used. From here, the positions of the outermost wind turbines of each wind farm cluster were used to limit the area as presented in Table 1. The regions R2 (south of the lidar location) and R5 (northwest) are not influenced by upstream wind farms. Region R1 (east) is influenced by the wind farms Gode Wind 1 and 2. Region R3 is influenced by the wind farm Nordsee One and region R4 by the wind farm cluster N-2 composed of the wind farms Trianel Borkum, Merkur, alpha ventus, and Borkum Riffgrund 1 and 2 (see Table 2 for a summary of the key characteristics of the wind farms surrounding the scanning lidar measurements).

After dividing the measurements into different regions based on wind direction, the lidar data have been further divided into subsets of atmospheric stability, which is expected to strongly affect the wind speed downstream due to the presence of far-field wind farm wakes (Cañadillas et al., 2020).

Table 1. Ranges of the individual wind sectors (regions) and distances based on the measurement location of the scanning lidar system.

Region	Sector boundaries [°]	Distance to lidar meas. point [km]
R1	[24, 170]	1.5
R2	[170, 186]	(free wind)
R3	[186, 235]	8
R4	[235, 277]	20
R5	[277, 24]	(free wind)

In this study, we use the static atmospheric stability, which only takes into account buoyancy effects and is characterized through the lapse rate (γ) based on the temperature gradient at two different altitudes, sea surface temperature (SST) and air temperature at the height of the transition piece (23.3 m) corrected for air pressure and density effects to obtain the virtual potential temperature (θ_v) gradient,

$$\gamma = \frac{d\theta_v}{dz} \approx \frac{\Delta\theta_v}{\Delta z}, \quad (1)$$

with z the measurement height. Negative values of the virtual potential temperature gradient γ, or lapse rate, represent an unstable stratification of the atmosphere; positive values represent a stable stratification; and values around zero represent a neutral stratification. The stability classes were chosen as follows:

- $\gamma < -0.04$: unstable stratification,
- $-0.04 \geq \gamma \leq 0.04$: near-neutral stratification,
- $\gamma > 0.04$: stable stratification.

A thorough discussion of different parameters used to characterize stability and the influence on wakes is provided by Platis et al. (2021), who use similar values to classify atmospheric stability based on lapse rate. Ideally, it would be optimal to measure the air temperature at hub height or above, but due to the lack of measurements and considering that the air temperature measurements at the nacelle are highly biased due to the rotor effect, we consider our estimation to be suitable as a first-order approximation for the framework of this study.

2.1 Scanning wind lidar

Wind data were recorded with a long-range-scanning Doppler wind lidar system of the type Streamline XR manufactured by Halo Photonics, UK (METEK-GmbH, 2021). The lidar system emits short laser pulses into the atmosphere and detects the radiation backscattered by aerosols

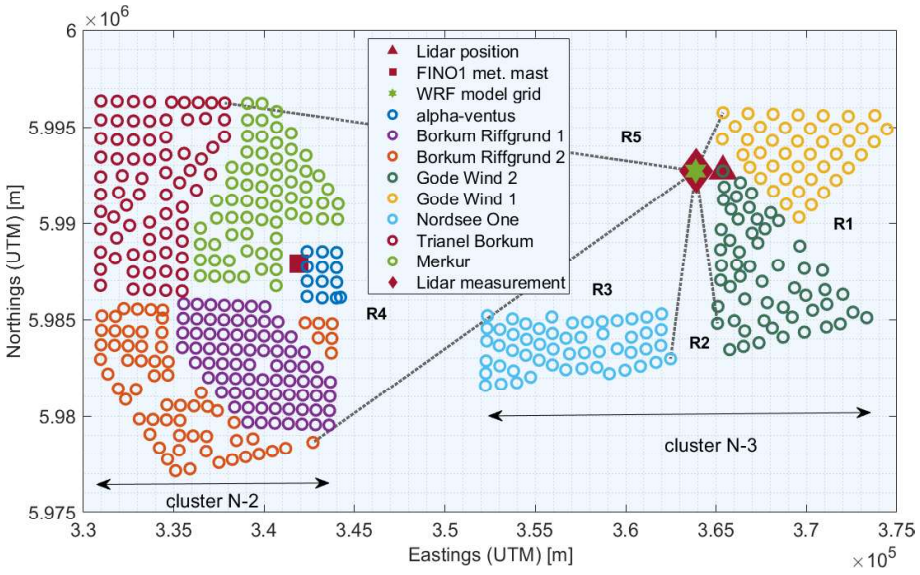

Figure 1. Location of the scanning lidar between the wind farm clusters showing the five sectors (from R1 to R5) into which the data are grouped for the analysis (dashed black lines). The individual wind turbines are represented by circles, and each individual wind farm is shown in a different color. The location of the meteorological mast FINO1 is also indicated (red square). The WRF model grid point investigated in this study is marked with a green star. Lidar system and lidar profile measurement locations are marked with a red triangle and a red diamond, respectively. Coordinates refer to UTM WGS84, zone 32.

Table 2. Properties of the wind farms (as of May 2020) surrounding the scanning lidar measurement. The cluster name is defined by the German Federal Hydrographic Agency BSH, wind turbine (WT) type within the wind farms, WT rated power (P_{rated}), their rotor diameter (D), hub height (h) for LAT (lowest astronomical tide) and the number of wind turbines (No. of WTs).

Cluster	Wind farm	WT type	P_{rated} [MW]	D [m]	h [m]	No. of WTs
N-3	Gode Wind 1 and 2	Siemens	6	154	110	55/42
N-3	Nordsee One	Senvion	6.2	126	90	54
N-2	Alpha ventus	Senvion/Adwen	5	126/116	92/90	6/6
N-2	Borkum Riffgrund 1 and 2	Siemens/Vestas	4	120/154	83	78/56
N-2	Trianel Wind Farm Borkum 1 and 2	Adwen/Senvion	5, 6.3	116/164	87/111	40/32
N-2	Merkur	GE	6	150	102	66

through optical heterodyning. This makes it possible to determine both the intensity of the backscattered radiation and its Doppler shift in the line-of-sight (LOS) direction, which is proportional to its radial wind speed, also called LOS wind speed.

The lidar system (see Fig. 2) was installed on the transition piece (TP) of the northernmost wind turbine (K01) of the wind farm Gode Wind 1, at a height of approximately 23.3 m LAT (lowest astronomical tide) and positioned on a metal support structure for a clear view in the azimuthal range [160°, 20°] over the railing to the west. In addition to the scanning lidar device, other sensors for collecting thermodynamic data (namely air temperature and humidity, pressure, precipitation, and water surface temperature) were installed. The purpose of these measurements was to characterize the atmospheric stability regime with the method previously described. The thermometer and hygrometer were mounted on a 50 cm long boom at a height of 22.5 m LAT, and the barometer was located in the control cabinet 50 cm below. The infrared sensor for measuring the SST was located on the railing of the TP and consists of a pair of sensors, with one sensor pointed towards the sea surface and the other towards the sky, which allows the temperature measurements to be corrected for the effects of background radiation (refer to Frühmann et al., 2018, for further details).

The lidar system, with a maximum range of 10 km, was set up with a gate length of 120 m. The sampling rate of the back-scattered signal of 50 MHz gives a spatial resolution of 3 m along the LOS. Furthermore, the accumulation rate can be reduced so that the highest beam sampling rate is 10 Hz. The laser beam is directed by a scanner with an arrangement of mirrors with 2 degrees of freedom, allowing scanning in all directions. The positioning of the scanner at the top of the lidar container box enables scanning of the sky above and a

Figure 2. Long-range-scanning lidar and additional measurement systems (on the right side) on the TP of one of the northernmost wind turbines (K01) at the wind farm Gode Wind 1.

Table 3. Overview of scanning lidar set-up during the measurement campaign.

Parameter	Value
Target distance [m]	1500
Target heights [m]	40, 80, 120, 160, 200
Elevation angles [°]	0.64, 2.17, 3.70, 5.22, 6.77
Azimuth sectors [°]	230° ± 7.5° and 300°±7.5°
Scan duration [s]	75
Scan speed [° s^{-1}]	3.17
Accumulation time [s]	0.6
Range gate length [m]	120

reduced area below the horizontal, without interference with itself.

The lidar performed plan position indicator (PPI) scans (at five elevations) with continuous scanner movement in two azimuthal sectors of 15° width upstream of the wind turbine K01. An overview of the lidar set-up is given in Table 3.

The set-up enabled the measurement of the wind profile in the vicinity of the wind farm Gode Wind 1 (approximately 1.5 km west of the wind turbine K01). To derive vertical profiles, we generate a so-called partial velocity azimuth display (VAD) plot at several altitudes using a sinusoidal function fitted to radial velocity data (Werner, 2005), which is represented as a function of azimuth. Then the results are calculated in terms of the Cartesian velocity components (u, v, w), and finally the wind speed and direction are derived. The classical approach relies on four radial velocities measured at constant elevation and in four quadrants in the azimuth around the lidar. In our approach, we rely on several radial velocities measured continuously on a limited area in azimuth and constant elevation to avoid measurements influenced by the wake of the wind farms Gode Wind 1 and 2. The general sketch of the approach in Fig. 3a shows how data are selected for the VAD plot near a target point and for several heights (panel b). After selecting data for an altitude, a check is made to see if the data meet a minimum carrier-to-noise ratio (CNR), and then a sine function is fitted using random sampling consensus (RANSAC) (Fischler and Bolles, 1981). This last method is used to avoid the remaining outliers and to increase the robustness of the fitting procedure.

As the lidar was positioned west of Gode Wind 1, the scanning was performed to the western side, targeting five heights above LAT, namely at 40, 80, 120, 160 and 200 m. In this free sector, we followed the scanning trajectory shown in Fig. 4a and with the scanner set-up shown in Table 3. In Fig. 4b, an example of the VAD results for the wind speed and wind direction for 1500 m and a height of 120 m is shown. In practice, every time a scan is finished, i.e., every 75 s (see key scanning parameters in Table 3), a VAD is performed and wind speed and wind direction at all five heights are stored. Finally, these data are averaged over 10 min.

An important point to consider when measuring wind with a lidar system is the orientation of the system. Orientation errors in the scanning lidar affect the exact position at which the wind is interrogated by the laser beam. Three angles are used to fully define the orientation of the lidar in three-dimensional space, namely bearing, tilt and roll. The further the distance to the lidar, the larger the error in positioning is, due to errors in one of these angles. It is therefore necessary to determine these angles at very high accuracy in order to reduce and properly quantify the positioning uncertainty. While the offset in the azimuthal direction between the geographic north and the lidar's north mark can be determined with a compass, this is very inaccurate for the site installation because the turbine structure affects the magnetic field around the lidar. A better option is to use the lidar itself and neighboring turbines of which their position is known ("hard targeting"). In this study, we target turbines of the neighboring wind farm Nordsee One at distances between 8 and 10 km and identified them by their very high backscattered signal with an accuracy of at least 0.1°. In addition, the system is equipped with an internal inclinometer, which is used to quantify tilt and roll. However, the manufacturer does not provide calibration information for this sensor. Furthermore, due to the high relevance of these angles, it is desirable, if not mandatory, to perform an on-site assessment of mounting errors and inclinometer performance. For this purpose, we apply the so-called sea surface leveling (SSL) proposed by Rott et al. (2022) during the commissioning of the lidar system at the offshore site. In this procedure, the sea surface is used as a reference to assess the orientation of the lidar system relative to the horizontal plane. Mainly, the scanning lidar, which is installed several meters above the sea, is set to perform a scan with constant downward elevation and constant azimuth velocity. In this set-up, the backscattered lidar signal describes the surface of a cone that extinguishes by absorption as it enters the water. The geometric analysis of

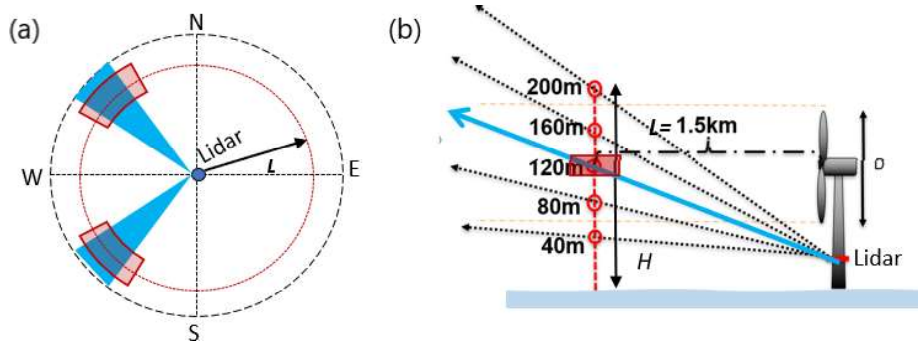

Figure 3. **(a)** Sketch of scanning for partial VAD. Shaded areas in blue represent areas where the wind is interrogated continuously. Areas in red represent the volumes where data for VAD are selected. **(b)** Sketch of the vertical profile of the wind speed and wind direction at the five target heights selected in this campaign, where L is the distance from the lidar system to the measurement location.

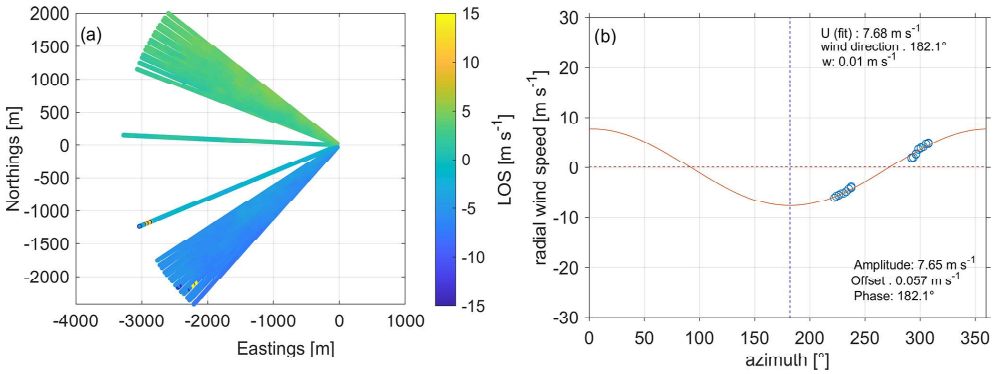

Figure 4. **(a)** Example of the top view of the radial wind speed (u_r) for a single full scan taking approximately 75 s on 29 August 2020. Eastings and northings are given in meters and relative to the lidar position. **(b)** Example of VAD data selected from the scan in **(a)** for a distance of 1500 m ±150 m and a height of 120 m ±5 m. The bottom legend shows results for the radial wind speed fit. The top legend indicates results of the wind speed.

the elliptical shape of the intersection of the cone with the water surface (see Fig. 5) provides the tilt and roll angles of the cone axis and thus of the lidar itself.

We adopt the results of the SSL method as a reference because they show the misalignment of lidar, scanner and support structure combined in a direct way. For this reason, the misalignment results from the SSL can be used in trajectory planning. Eventually, the data could also be used to calibrate the internal inclinometer or any other auxiliary inclinometer used in a campaign. The SSL is performed regularly to check if the alignment has changed.

To assess the robustness of the SSL and its performance against the internal inclinometer of the scanner system, we ran the SSL continuously for almost 18 d from 6–24 August 2020. Figure 6a and b show, respectively, the time series of tilt and roll obtained from the SSL and the internal inclinometer. Each time step represents the result of a full SSL scan (with a duration of about 2.5 min) and the corresponding mean value of the inclinometer data. In addition, the standard deviation of the inclinometer is shown as a band of $\pm\sigma$. The results show a good correlation between the two signals. The

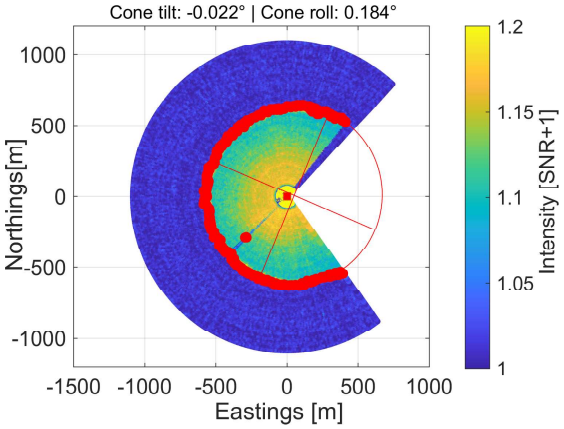

Figure 5. Example of backscattered signal intensity after SSL scanning. Red dots show the estimated water entrance. The red ellipse and its axes reveal a misalignment of the sensor. The blind area to the east is due to the turbine tower.

SSL indicates a different bias in each axis of the inclinometer, namely $\text{tilt}_{\text{bias}} = -0.05°$ and $\text{roll}_{\text{bias}} = +0.05°$. A change

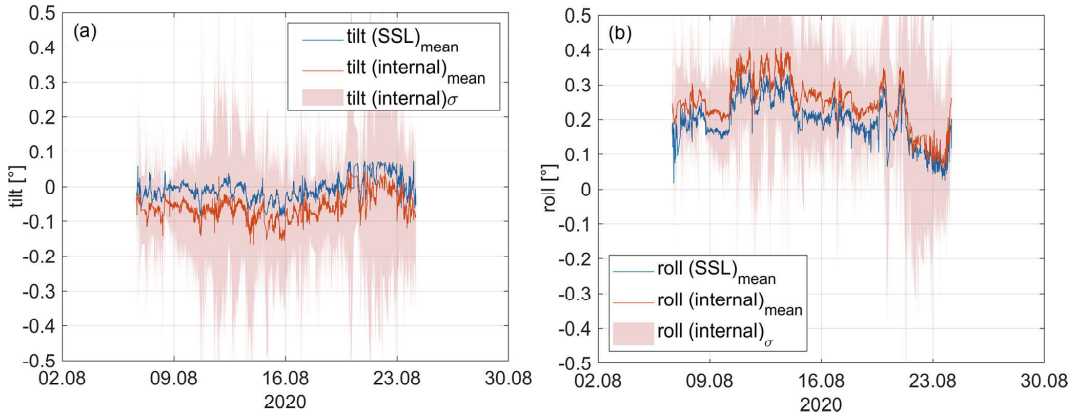

Figure 6. **(a)** Lidar tilt from internal inclinometer (internal, red) and from SSL (blue). The red band shows the standard deviation (SD) of the inclinometer tilt during each SSL scan. **(b)** Lidar roll from internal inclinometer (internal, red) and from SSL (blue). The red band shows the standard deviation (σ) of the inclinometer roll during each SSL scan.

in mean tilt and roll over time can be observed. This is due to the varying conditions of the support structure. In particular, the thrust of the wind turbine changes the magnitude and direction of the tower inclination depending on the wind direction and wind speed. The error between the two sensors (now assuming SSL as the sensor) can be seen in Fig. 6a and b. After debiasing both errors, we obtain mean-square errors of $\epsilon_{\text{tilt}} = 0.01°$ and $\epsilon_{\text{roll}} = 0.02°$. Finally, the variance of the inclinometer is a consequence of the system dynamics, which must be taken into account when assessing the accuracy of the scanner alignment. The total variance of the inclinometer signals is $\sigma_{\text{tilt}} = 0.23°$ and $\sigma_{\text{roll}} = 0.24°$. It should be noted that in the absence of information on the calibration of this sensor, we assume this value to be conservative. This is based on the assumption not only that the sensor perfectly detects rotational changes but also that the resulting values are a superposition of rotational and translational movements.

2.2 Mesoscale model

Mesoscale simulations, including both undisturbed free wind conditions and the wake-disturbed wind field due to the surrounding wind farm, were performed using the WRF model (version 4.2.1) developed by the National Center of Atmospheric Research (Skamarock et al., 2019). In the WRF model, there are prognostic variables for the horizontal and vertical wind components, potential temperature, geopotential and surface pressure of dry air as well as several scalars such as cloud water and water vapor. The WRF model is well known and widely used in the wind energy community (Huang et al., 2014; Hahmann et al., 2020; Kibona, 2020), and in recent years also for wind farm wake simulations (Pryor et al., 2019; Siedersleben et al., 2018b).

Our set-up was optimized within several research projects for wind energy applications, especially with a focus on offshore conditions (Gottschall et al., 2018; Dörenkämper et al., 2020; Gottschall and Dörenkämper, 2021). The studies by Gottschall et al. (2018) and Gottschall and Dörenkämper (2021) compare the mesoscale model data from a similar set-up against vertical lidar and mast measurements. The WRF model set-up is based on the extensive sensitivity studies carried out in the framework of the NEWA (New European Wind Atlas) project (Hahmann et al., 2020; Dörenkämper et al., 2020). The final set-up was validated against almost 300 masts in different terrain complexity. In low terrain complexity this set-up showed a bias of the mean wind speed of $0.06\,\text{m}\,\text{s}^{-1} \pm 0.49\,\text{m}\,\text{s}^{-1}$ evaluated at 110 masts. To limit the number of grid points in the numerical calculations, a nesting technique is used. Three domains centered around the German Bight area are nested, each of a size of 120 grid points with resolutions of 18, 6 and 2 km. Figure 7a shows the distribution and size of the three domains around the site of interest.

The wind turbines were parameterized as momentum sinks and source of turbulence using the Fitch wind farm parameterization (Fitch et al., 2012). In every grid that intersects the rotor disk, the horizontal wind components are reduced to represent the drag of the wind turbine. Different thrust and power curves corresponding to all turbine types were applied. Figure 7b shows the locations of the turbines in the model simulations. Boundary conditions for the model were prescribed by the ERA5 dataset (ERA5 resolution, $0.25° \times 0.25°$ (~ 30 km), 6-hourly) for the atmospheric variables (Hersbach et al., 2020) and the OSTIA dataset for the sea surface variables (Donlon et al., 2012), which provides near-real-time global sea surface temperature at the grid resolution of $1/20°$ (~ 6 km). The WRF version used in this study does account for the turbulent-kinetic-energy advection bug that was recently discovered (Archer et al., 2020).

We performed simulations with and without wind farms and extracted the time series from the WRF simulations at the position of the scanning lidar measurements for the same

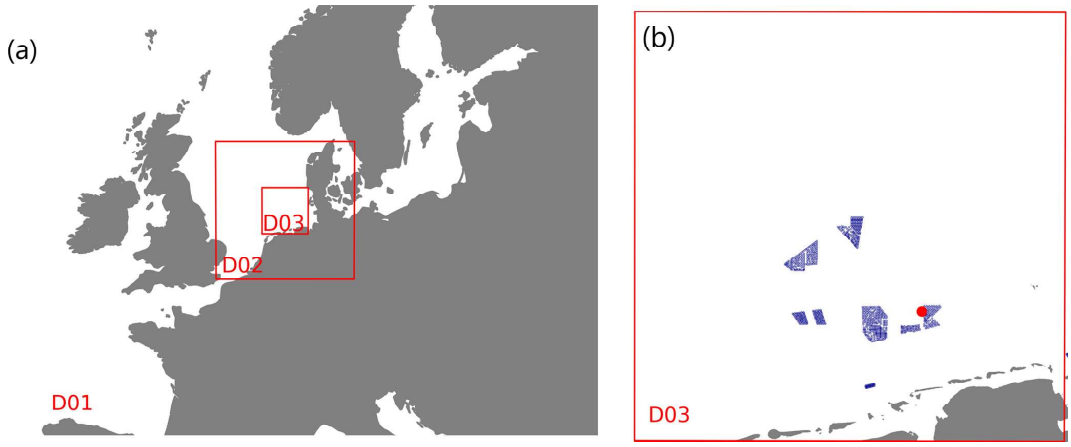

Figure 7. **(a)** Locations of the three WRF model domains (D01, D02, D03) with a grid sizes of 18, 6 and 2 km, respectively. The innermost domain (D03) of **(a)** is shown in detail in **(b)** with the locations of the wind turbines accounted for in the simulations and the location of the lidar measurements marked in red. Note that wind farms with a distance of more than 100 km from the site were ignored.

period. The most important settings of the mesoscale model configuration are summarized in Table 4.

2.3 Airborne measurements

The spatial extent of the wind farm wakes can be briefly investigated by considering one of the measurement flights carried out during the scanning wind lidar measurement period with the research aircraft Dornier DO-128 operated by the Technische Universität Braunschweig (Lampert et al., 2020).

Although the flight data are limited to a few hours within a single day, they provide an overview of the wind situation at different distances and vertical profiles both upstream and downstream of the wind farm clusters. The research aircraft is equipped with a nose boom to perform high-resolution measurements of the wind vector, temperature, humidity and pressure, sampling at a frequency of 100 Hz (Corsmeier et al., 2001). Sensors for measuring the surface temperature, a laser scanner for determining sea state characteristics and cameras were also integrated (Lampert et al., 2020). During the measurement flights, both the upstream and downstream areas of the wind farm clusters were investigated. The flight pattern included legs of 45 km length that were aligned perpendicular to the main wind direction, therefore crossing the wakes, and vertical profiles from around 15 m altitude up to 1000 m. The individual straight flight legs were horizontally spaced about 10 km from each other. The measurement height was 120 m above sea level, which corresponds to the hub height of the wind farms Gode Wind 1 and 2.

An example of a flight dataset showing multiple wake-transect profiles perpendicular to the mean wind direction, measured downstream of clusters N-2 and N-3 on 3 July 2020, is briefly presented in the next section.

3 Wind field modification by wind farm clusters

The strong modification of the wind field by the wind farm clusters is clearly evident in scanning lidar measurements, flight measurements and WRF simulations. Flight measurements enable an initial side-by-side evaluation of the WRF model over a larger spatial scale than is possible with just the scanning lidar system and illustrate the strength and extent of wind farm cluster wakes (Sect. 3.1). The lidar measurements are then compared with WRF model results with and without a wind farm parameterization for the different sectors and atmospheric stability conditions, which enables an evaluation of WRF performance for different upstream wind conditions (Sect. 3.2).

3.1 The spatial extension of cluster wakes

Because of the extended range of flight paths around the wind farm clusters, the flight measurements are presented here to complement the lidar measurements. We consider the wake situation of the N-2 and N-3 clusters on 3 July 2020 (10:24–13:02 UTC) when flight legs were performed perpendicular to the mean wind direction ($\approx 230°$) and taking on average 10 min per traversal. The cluster wake limits in Fig. 8a are defined as the physical cluster extent which expands with distance x at the rate of $k_w = 0.04$ (wake decay constant for offshore as suggested by Sørensen et al., 2008.

The spatial distribution of the measured wind speed is inferred in Fig. 8a from the flight legs extending perpendicular to the wind direction. Darker colors, representing lower wind speed values, are evident directly behind the wind farms and more dense clusters of wind turbines. In particular, the strong reduction in wind speed downstream of cluster N-2, which is located to the west, but also the wind farms Gode Wind 1 and 2, which are located further to the east, can be clearly seen. Behind the northeastern edge of Gode Wind 2, the wind

Table 4. Relevant parameters of the mesoscale model set-up. The references for the different schemes and models are summarized in WRF Users Page (2020).

Parameter	Setting
WRF model version	4.2.1
Planetary boundary layer (PBL) scheme	MYNN level 2.5
Wind farm parametrization	Fitch et al. (2012)
Land use data	MODIS
Surface layer scheme	MYNN
Microphysics scheme	WRF single-moment five-class
Shortwave and long-wave radiation	RRTMG
Atmospheric boundary conditions	ERA5
Sea surface conditions	OSTIA
Horizontal resolution	18, 6 and 2 km
Vertical resolution	60 eta level
Nudging	Grid nudging above PBL
Model output interval	10 min
Nesting	One-way
Land surface model	Unified Noah Land Surface Model
Simulation duration	240 (+24 spin-up) hours

speed is about 7.5 m s^{-1}. Upstream of the wind farm, the wind speed is about 11 m s^{-1}, which corresponds to a reduction in wind speed of about 30 %. Stability during this period was inferred from vertical temperature profiles outside the wake area influenced by the wind farm clusters by steep climbing and descending flight profiles up to an altitude of about 1000 m, which reveal, after an initial close-to-neutral period (−0.005 K m^{-1}), stable conditions (with a maximum value of 0.01 K m^{-1}) for the last legs and thus explain the strong wakes detected.

Figure 8b shows the horizontal wind speed transect for the closest flight traversal (black line) upstream of the lidar measurement point ($x = -0.33$ km) compared with the mean wind speed according to the lidar (green diamond) and standard deviation for the duration of the flight leg (error bars), revealing a suitable agreement between the two measurements for this flight (mean bias = 0.06 m s^{-1}). For this leg, the lapse rate was −0.003 K m^{-1}, implying neutral conditions, which explains the relatively high turbulence signal in the 100 Hz data (gray line). The flight leg was performed between 11:27 and 11:37 UTC.

For comparison, the WRF-WF model results for the times 10:00 (red dotted curve), 11:00 (blue dotted curve) and 12:00 (purple dotted curve) UTC are shown for a transect corresponding to the flight coordinates. Note that for this particular time period, there is an approximate time delay of around 1 h, which is common in WRF results. The flight altitude corresponds to approximately 120 m, corresponding to the mean hub height of the N-2 and N-3 clusters and the mean wind direction of 228° for this transect. While these data also show a decrease in the wind speed between the limits of the cluster N-2, the wind speed of the wake minimum is about 0.5 m s^{-1} higher than the flight leg. The mean wind direction difference between the flight leg and the simulation is about 10°. It is worth mentioning that the WRF simulation does not take into account the wind farms located at about 15 km east of the cluster N-2 (Gemini wind farm), which could explain the difference of more than 1 m s^{-1} at the northern part of the wind farm wake (negative x axes).

Figure 9 shows the WRF-model-simulated horizontal wind field with the wind farm parameterization at mean hub height (120 m) and at different time steps.

Both the observations (Fig. 8a) and model (Fig. 9) show a wake extending at least 40 km downstream of the N-3 wind farm cluster, meaning this wake was long enough to reach the wind farm cluster N-4 (not shown) located about 60 km downstream of Gode Wind. In the spanwise direction, the wake has dimensions of approximately the maximum width of the wind farms. The simulations for different time steps indicate the temporal variability of the wind field well, which has to be considered for a flight duration of 4 h as well. As shown next, significant wake effects were detected by the scanning lidar for cases such as these for flow from the east.

3.2 Directional and stability dependence of cluster wakes

We evaluate the lidar-derived wind speed measurements by first dividing the wind direction into five unequal sectors within the cluster wakes (see Fig. 1). The lidar measurements are then compared with mesoscale model results without and with a wind farm parametrization for the different sectors, which enables (1) an estimation of the wind speed deficit when using the model without wind farm parametrization and (2) an evaluation of the model (with wind farm parametrization) performance for the different upstream conditions. Note that because the stability is also wind direction

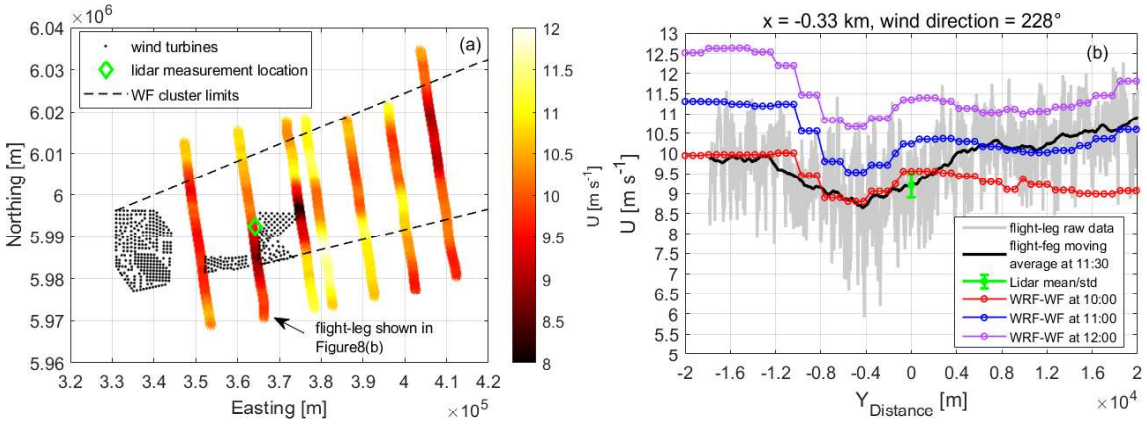

Figure 8. **(a)** Flight path in the vicinity of the clusters N-2 and N-3 (individual turbines as black points) of the measured wind speed from the measurement flight on 3 July 2020 (10:24–13:02 UTC). The black dashed lines indicate the downstream boundaries of the clusters for the measured wind direction of 230°. The flight altitude during the traversals of the wake clusters was ≈ 120 m, and the coordinates refer to UTM WGS84, zone 32. **(b)** Horizontal wind speed transect for the closest flight traversal upstream of the lidar measurement point ($x = -0.33$ km, where the negative sign refers to the left of the location of the measurements obtained by scanning lidar) and perpendicular to the wind direction. The gray line represents the 100 Hz data, the black line shows the data filtered by a moving average and the green diamond with error bars represents the lidar mean wind speed and its standard deviation for the duration of the flight leg (≈ 10 min). The red, blue and purple dotted lines show the WRF results with a wind farm parameterization (WRF-WF) from a transect of the model results at 10:00, 11:00 and 12:00 UTC, respectively, based on the flight coordinates.

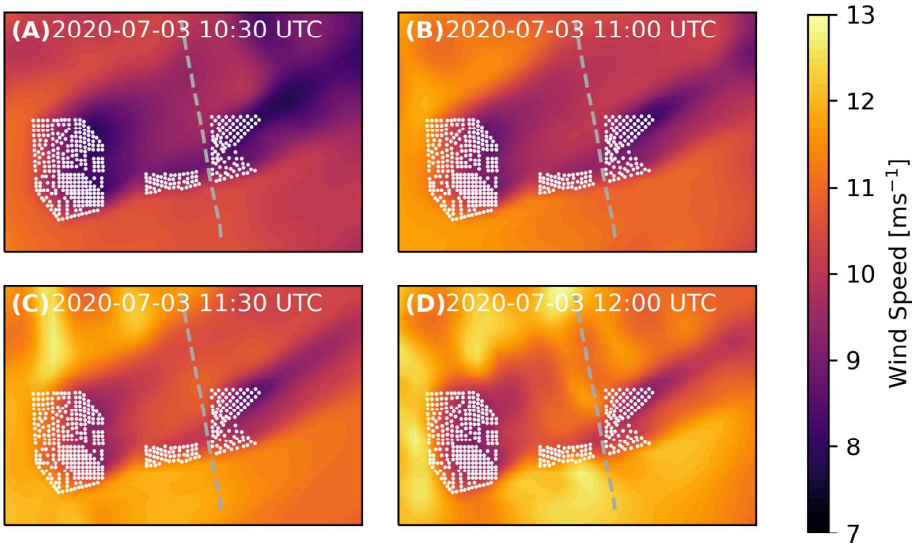

Figure 9. Spatial distribution of the modeled wind speed (see color bar) from the WRF simulation with a wind farm parameterization on 3 July 2020 at different time steps. The dashed gray line indicates the position of the flight leg shown in Fig. 8b.

dependent at this site, some sectors are affected more by certain stability conditions.

Figure 10a shows the wind rose from the lidar measurements together with the five wind direction regions R1–5, illustrating the predominance of a west-southwesterly wind direction for the data period presented here, which corresponds to the main meteorological wind direction in the German Bight area (Cañadillas et al., 2020). Figure 10b shows the Weibull distribution for the wind speed together with the scale parameter A and shape parameter k for each region R1–5 at 120 m. This illustrates that meteorological conditions and wind speed distributions within a region are very different, so that a direct comparison of wind data between the different sectors does not make sense due to the different flow conditions found in each sector. (For a more detailed depiction of the lidar data distribution for different sectors, please refer to Appendix B.)

The wind roses derived from lidar data for different atmospheric stabilities are shown in Fig. 11, illustrating that a large part of the data obtained during stable atmospheric

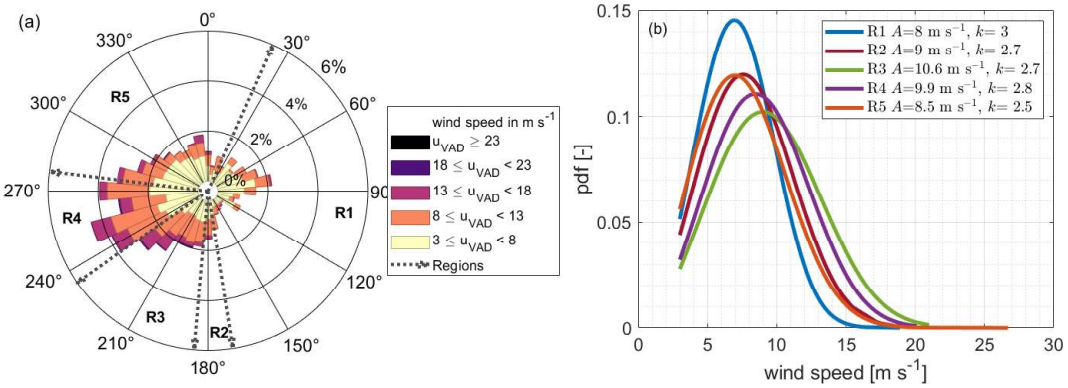

Figure 10. Wind rose **(a)** and Weibull distribution per regions R1–5 **(b)** at 120 m altitude measured by the scanning wind lidar for the period from May to September 2020.

stratification correspond to flow from the east. With neutral atmospheric stability, southwesterly winds prevail, while in unstable stratification northwesterly winds are predominant. Unstable and neutral conditions are associated with higher average wind speeds than stable conditions.

The wake-induced wind speed reduction at the position of the lidar measurements is investigated for each wind region using a polar plot for which the mesoscale simulation results (without wind farm parameterization) are used as the reference free wind speed. Since the model data represent an undisturbed state not influenced by wind farms, differences in the wind conditions are to be expected when comparing the two datasets. Especially in the regions R1, R3 and R4, which are directly influenced by the wind farm clusters, lower measured wind speed values are expected. Figure 12 shows the direct comparison of the wind speed values per wind direction of the lidar and the mesoscale model data at 120 m height for (a) unstable, (b) neutral and (c) stable atmospheric conditions. To aid visualization, the boundaries of the regions R1 to R5 and the individual positions of the wind turbines are also indicated.

Relatively good agreement is found between both datasets in unstable conditions and in region R2 in neutral conditions. The difference in wind speed in the other regions is also minimal under unstable stratification where the influence of the wind farms is difficult to detect in the measurements since wind farm wakes are not expected to be large. In contrast, a comparison of the datasets for neutral and stable atmospheric stratification shows a clear discrepancy between the measurements and model results, with this difference particularly evident in the regions R1, R3 and R4, which are directly influenced by wind farm clusters. The maximum difference is about 4 m s^{-1} in region R3 in stable stratification. Even with neutral stratification, a difference can be seen in the two wind speed datasets and the regions influenced by wind farms. In the free-wind region, however, both datasets agree very well. The strong fluctuations in the wind speed of the lidar data in region R1 are due to the very small amount of data in neutral stratification (see Fig. 12). For region R5, in the case of stable atmospheric stratification, there are no or too few data available in some wind direction sectors. A comparison of the data from the free-wind sector is not possible here. Nevertheless, the reduction in wind speed caused by the wind farms in the other regions can be clearly seen.

To quantify the effects of the wind farm wake in the different regions, the wind speed deficit (ϵ_{WRF}) of the lidar-measured wind speed u_{lidar} with respect to the mesoscale wind speed u_{WRF} is defined as

$$\epsilon_{\mathrm{WRF}} = \left(\frac{u_{\mathrm{lidar}}}{u_{\mathrm{WRF}}} - 1\right) 100\,\% \tag{2}$$

and presented in Fig. 13a, which is computed as an average over all points in each wind direction region for unstable, neutral and stable conditions. The bars within a group represent the five measurement heights of 40, 80, 120, 160 and 200 m, and the number of 10 min lidar values within a bar is shown at the end of the bar.

The wind speed deficit ϵ_{WRF} in region R5, the free-wind region, is small for neutral and unstable conditions ($< 10\,\%$), especially for unstable stratification (1 %–2 %), for all measurement heights. For the second free-wind sector R2, only small differences between the WRF model and lidar data are evident in the case of unstable and neutral atmospheric stratification. However, the results in this sector vary strongly with height. One possible reason for this is that the lateral extent of the narrow undisturbed corridor in region R2 is too small, only about 3 km, and that the boundaries of the wake effects become wider with increasing distance to a wind farm due to the wake expansion. This effect is enhanced by a stable atmosphere. Even when the corridor was further narrowed by changing the region boundaries of R2, no effect similar to R5 was detected. The small horizontal extent of the corridor and the large distance of the lidar measurement site from this area make a differentiated evaluation of region R2 difficult.

The regions R1, R3 and R4 influenced by the wind turbines all show a relatively large wind speed deficit. As ex-

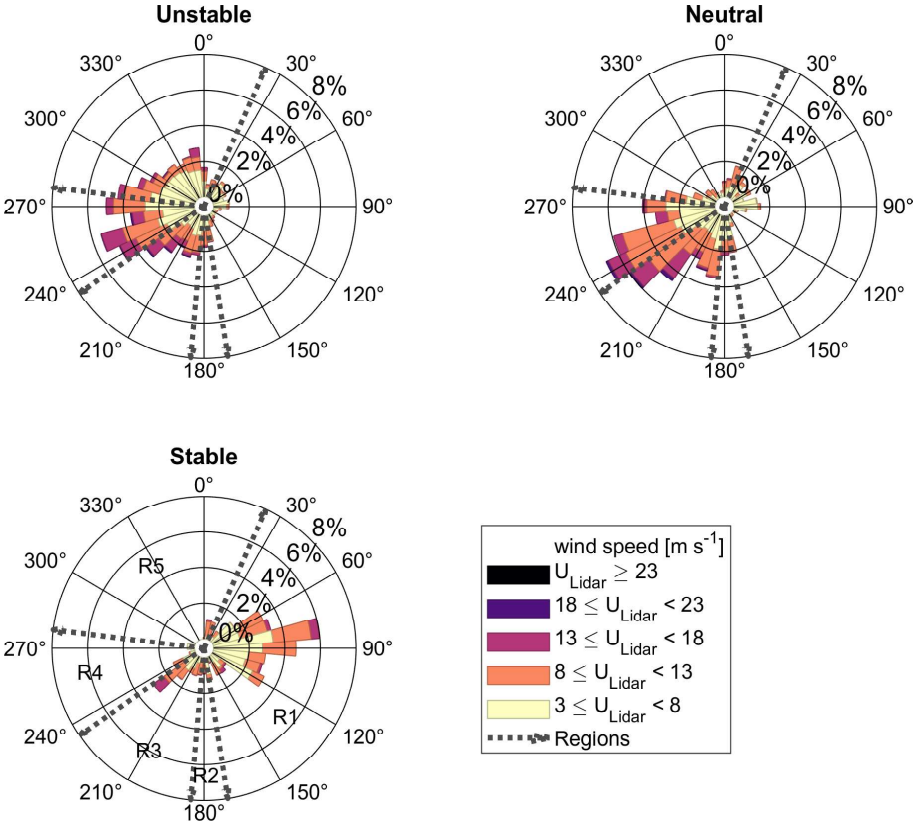

Figure 11. Wind roses measured by the scanning lidar for different atmospheric stabilities at 120 m above LAT. The regions R1–5 are indicated by dashed lines.

pected, the ϵ_{WRF} values measured are generally lower (negative) than the values from the undisturbed computational model at all heights and stability conditions, particularly in stable stratification. In region R4 and at a measurement height of 120 m, $\epsilon_{WRF} \approx -30\,\%$ in stable stratification. It is also noticeable that the reduction in wind speed shows a negative trend with increasing height. While the maximum height of the lidar measurements may be 200 m and most of the wind turbines in the surrounding area have a total height between 140 and 180 m, some interaction effects can also be detected above the wind farm due to vertical wake expansion (Siedersleben et al., 2018a; Larsén and Fischereit, 2021). However, as measurements at a height of 200 m are only partially influenced by the wind turbines, as they are no longer completely behind the rotor surface, this probably explains the lower wind speed deficit at 200 m.

The wind speed differences can be further emphasized for different atmospheric stability conditions within a region. Here it is noticeable that, in regions R4 and R3, a strong reduction in wind speed behind the wind farms with increasing atmospheric stability can be seen, but this is much less pronounced in region R1. As regions R3 and R4 have a larger distance to the measuring point of the lidar than region R1, it can be assumed that, in an unstable atmosphere, the wind speed recovers more quickly in the wake of a wind farm than in stable conditions, as also shown in Cañadillas et al. (2020).

The lateral extent of a wind farm, i.e., the number of wind turbines in the flow direction as well as the wind turbine layout, also affects the strength of the change in wind conditions in the wake of a wind farm cluster. Region R3 is influenced by the wind farm Nordsee One. Here, a maximum of six to seven wind turbines are located behind each other in the flow direction. In region R4, which is influenced by the wind farm cluster N-2, the number of wind turbines in the direction of flow is 17 to 20 turbines, depending on the wind direction. This effect is evident when considering the wind speed differences in regions R3 and R4 under unstable atmospheric conditions. Although the distance of the wind farm in region R3 to the measurement location of the lidar is significantly smaller, the reduction in wind speed is smaller than in region R4. A possible reason for this is the size of the wind farm cluster in R4.

Figure 14 shows a polar plot comparing WRF results, both without and with wind farms, with the lidar measurements, for all atmospheric stabilities detected during the measurement period. To ensure a fair comparison between the mesoscale (WRF-WF) model and the lidar, hourly production data from energy charts (available at https://www.

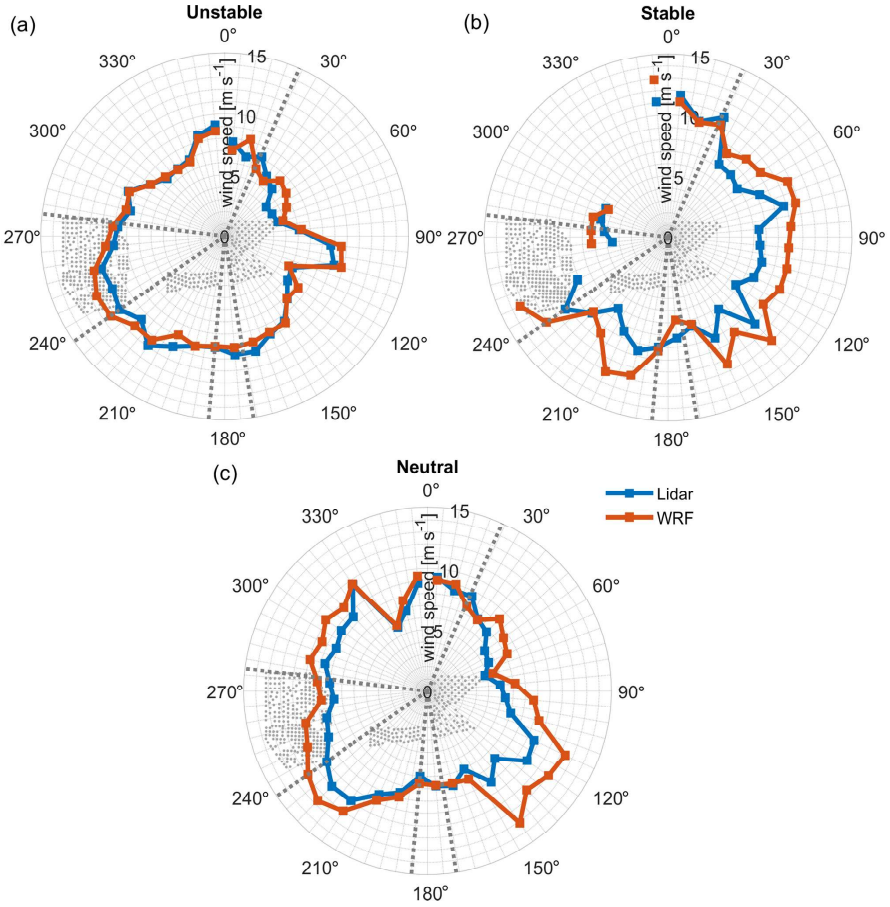

Figure 12. Wind speed polar plots of the lidar measurements and WRF results (without the wind farm parameterization) for **(a)** unstable, **(b)** stable and **(c)** and neutral atmospheric stratification at the height of 120 m. Wind turbines are indicated by gray points and the regions R1–5 by dashed gray lines.

energy-charts.de/, last access: July 2021) were used for filtering purposes. Only wind farms in operation at the measurement times are included in the mesoscale simulations and thus considered in the comparison.

Wind speed deficits of up to about 30 % are shown for the easterly winds at a distance of 1.5 km and up to 15 % for the southwesterly flow at a distance of about 20 km. On the other hand, the lidar (blue) and WRF-WF (green) data show improved agreement between the two datasets for all directions with a difference in wind speed of about 2 %, indicating that the WRF-WF model with the wind farm parameterization included is capable of capturing the mean wake effects detected by the in situ measurements.

As for Fig. 12, the data presented in Fig. 14 are divided into unstable (a), stable (b) and neutral (c) conditions in Fig. 15 for the WRF model with the wind farm parameterization (green line) and for the scanning lidar (blue line). A good agreement is found for most of the regions (R1, R4 and R5) under unstable conditions with a wind speed difference of around 2 % in wind speed. The larger disagreements in wind speed (almost 15 %–20 %) are found under stable conditions for the regions R1 (downstream of the large wind farm clusters Gode Wind, N-2) and R2 and of around 10 % for the region R3 (downstream of the relatively small wind farm Nordsee One).

Figure 13 (lower panels) also presents the wind speed difference for the mesoscale model $\epsilon_{\text{WRF-WF}}$. In general, the wind farm parameterization reduces the absolute magnitude of the wind speed difference $\epsilon_{\text{WRF-WF}}$ in the waked regions, especially for regions R1 and R4 to, respectively, the east and west of the lidar for all stability classes, and for region R3 to the southwest of the lidar, except for unstable conditions where the value of $\epsilon_{\text{WRF-WF}}$ is more positive for all heights. This could be due to coastal effects to the south not being properly captured by the model (see also the southern part of the polar plot in Fig. 15a). The difference in the narrow region R2 to the south is also worsened by the wind farm parameterization, including for all stability classes. Our lidar measurements thus serve as a reference for further improvements in wind farm parameterizations.

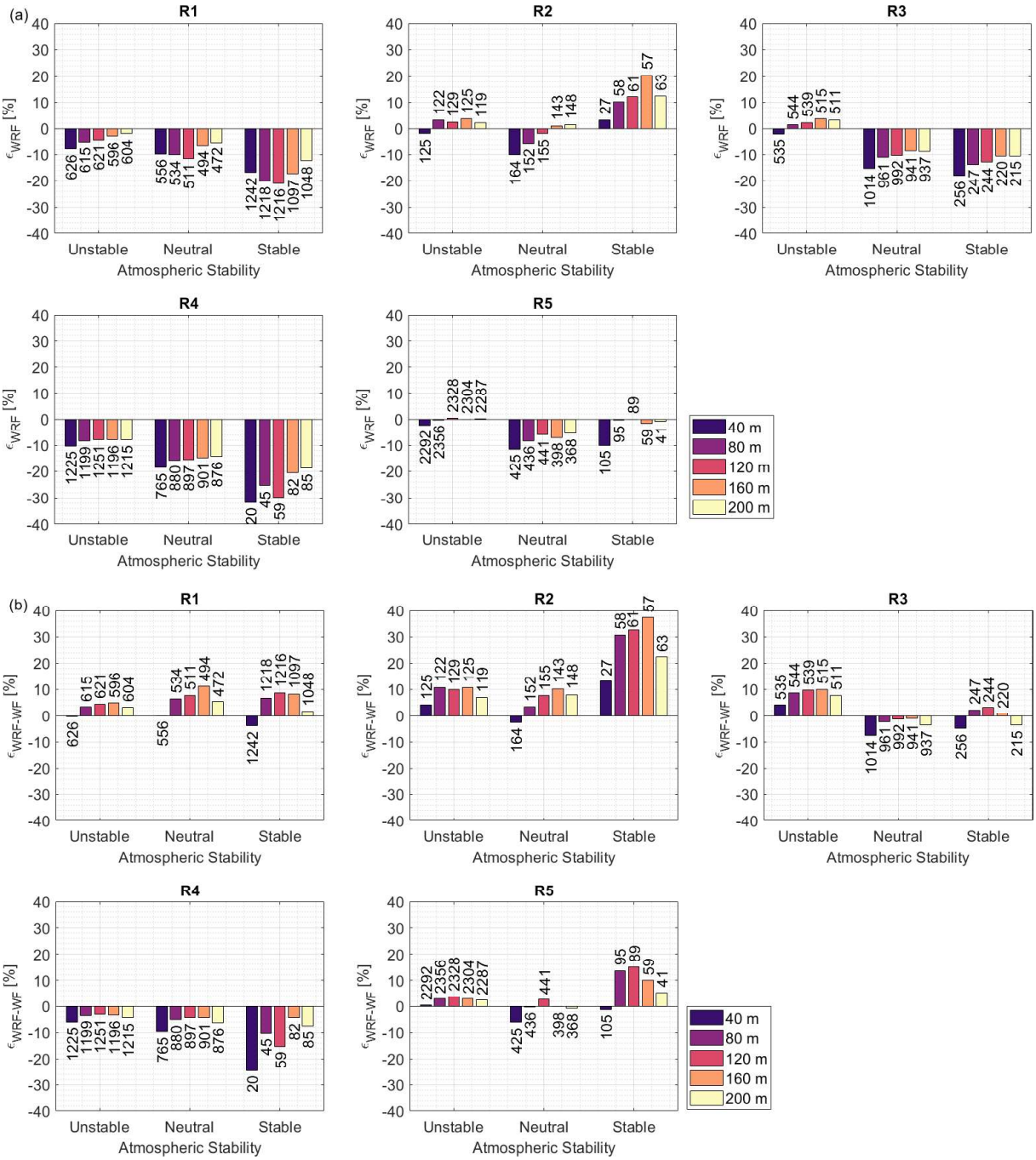

Figure 13. The deficit ϵ_{WRF} (Eq. 2) in the wind speed between the lidar measurements and WRF model for **(a)** no wind farm parameterization u_{diff}(WRF) and **(b)** with the wind farm parameterization $\epsilon_{WRF\text{-}WF}$ for regions R1 to R5; for each measurement height 40, 80, 120, 160 and 200 m; and for each stability class. The number below and above each bar indicates the number of 10 min wind speed values.

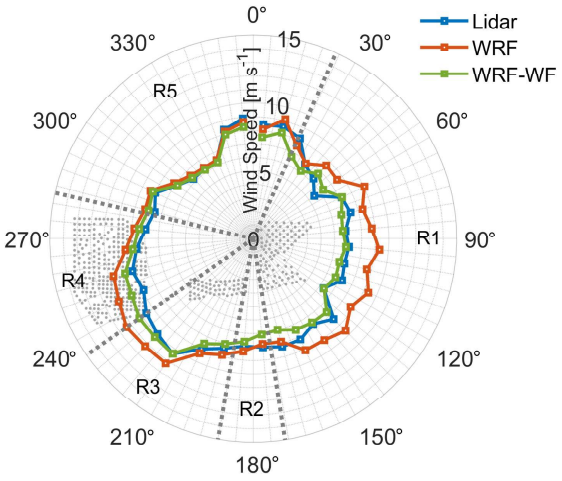

Figure 14. Wind speed polar plot of the lidar (blue) and WRF model without (red) and with wind farm influences (WRF-WF, green) at 120 m. Wind turbines are indicated as gray points, and the sectors are indicated as dashed gray lines.

4 Discussion

In this study measurements of wakes inside an offshore cluster are reported for the first time. Data of a lidar scanner installed on the transition piece of a wind turbine located within a cluster in the German Bight are collected and analyzed within a 5-month field campaign. As part of the goals of this study, a detailed description of the experimental setup and an uncertainty estimation have also been presented. We have implemented a method for obtaining a representative wind speed vertical profile with a single scanning lidar for areas nearby offshore wind farms. The method comprises two novelties in the application of scanning lidars offshore. First, we used a lidar VAD analysis to deliver wind characteristics in a domain between 1 and 2 km instead of concentrating on one-point measurements. Second, we used what we call partial VAD to derive area-equivalent wind speed and wind direction. We selected the area-equivalent approach to obtain more representative wind characteristics, especially across inhomogeneous flow. Moreover, we expected the spatial "averaging" effect to make the results more comparable to mesoscale models. The results presented in this paper support our hypothesis that such a measurement approach is also robust in wind farm wakes and can be applied for resource assessment. On the technical side, this is the first time, to our knowledge, that this type of scanning and data processing have been implemented. One usually obtains wind speed profiles with scanning lidars in the vicinity of wind farms using a dual-Doppler-lidar approach. This means that two scanning lidars operate simultaneously. With our approach we considerably reduce the campaign complexity and execution costs. This has advantages for the industry and is potentially an application for campaigns where fixed structures and existing infrastructure can be used to install the scanning lidar. Finally, this could be an alternative to floating lidars for some measurement campaigns near wind farms. Moreover, these systems can be relatively easily installed on the TP of an offshore wind turbine. So far, there is no standard similar to that existing for other remote sensing systems, for instance, vertical ground-based lidars (e.g., as part of IEC-61400-12). In addition to the scanning lidar, we describe a novel way to easily estimate the stability of the atmosphere by installing air temperature and sea surface temperature sensors on the railing of the TP. Normally, air and sea temperature and humidity are not measured in close proximity to wind measurements at offshore locations when using a lidar system. However, several previous studies have shown that the stability of the atmosphere plays a decisive role in the value of the wake deficit, so it is necessary to have an estimate of this parameter. We used a WRF model to estimate the wind deficit as no undisturbed wind measurements are available during the scanning survey campaign in the area, which is a general problem of such an inner wind farm cluster analysis. High-fidelity WRF model simulations are used to (1) estimate the average wind speed deficit and (2) compare the inter-wake effects simulated by the model with the scanning lidar data. Analyses are performed for different in-flow directions based on the obstacle encountered at the measurement position (i.e., a wind farm in the case of Nordsee One or a wind farm cluster) and for different atmospheric stabilities. For the comparison of measurements to the WRF model, 10 min time series of wind simulations were extracted at the position of the scanning lidar measurements and without taking into account the effect of the turbines on the model. We have demonstrated that our lidar measurements are able to quantify wake effects within a modern offshore cluster. The dependency of the results is plausible in the sense of external parameters like atmospheric stability.

5 Conclusions

Interaction effects between wind farm clusters N-2 and N-3 in the German Bight are demonstrated via the analysis of data from a scanning lidar, airborne measurements and a mesoscale model. Lidar measurements combined with meteorological sensors reveal the strong directional and stability dependence of the wake strength in the direct vicinity of wind farm clusters. For sectors without upstream wind farms, the scanning lidar data agree with the mesoscale simulations of the undisturbed flow in unstable, neutral and stable atmospheric conditions. In region R5 (sector free of wind farms to the north), the maximum wind speed deficit is about 2 %, whereas in region R4 a reduction of up to 30 % was observed. The magnitude of the deficit increases in all other regions with increasing atmospheric stability.

The wakes still have an influence at 200 m altitude, but it is much smaller than at hub height. This effect is also appar-

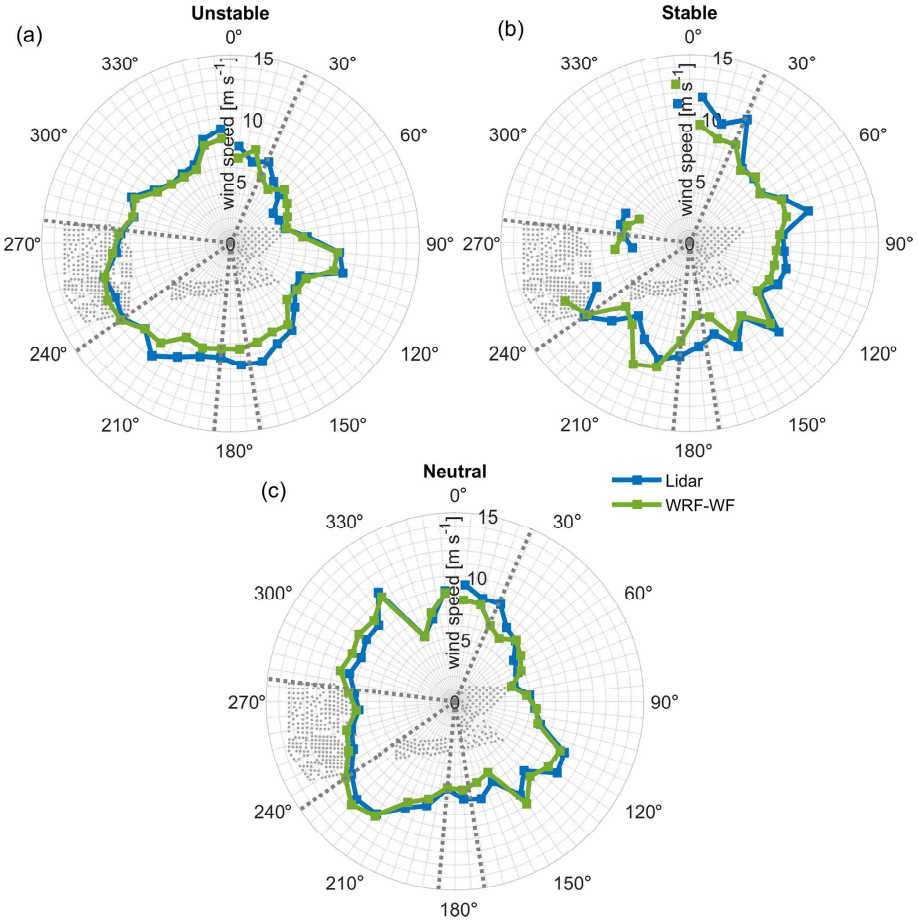

Figure 15. Wind speed polar plots of the lidar measurements and WRF-WF results (with the wind farm parameterization) for **(a)** unstable, **(b)** stable and **(c)** neutral stratification at the height of 120 m. Wind turbines are indicated by gray points and the regions R1–5 by dashed gray lines.

ent when examining the wind speed at other measurement heights.

This observational dataset allows for numerical model validations. Taking into account the mesoscale wind farm parameterization (WRF-WF), overall, the model performs reasonably well and is able to capture the wake trend. A good agreement is found for most of the regions (R2, R3 and R5) in unstable conditions, with a relative deviation of around 2 % in wind speed. As expected, the larger disagreements in wind speed (almost 20 %) are found for stable conditions for the regions R1 and R4, amounting to around 10 % for region R3. This means that mesoscale wake simulations still have deficiencies in correctly reproducing the atmospheric stratification and its influence on the development and decay of wind farm wakes. Scanning wind lidar measurements are therefore a powerful tool for the evaluation and improvement of wind model simulations and in particular wind farm parameterizations. We conclude that the scanning Doppler wind lidar is a flexible, accurate and robust tool for deployment inside wind farm clusters for the investigation of the flow phenomena therein. Further work is ongoing to establish longer-term measurement campaigns and comparisons with standard industry models.

Appendix A: Quantification of scanning wind lidar uncertainties

Any field measurement has inherent uncertainties which have to be estimated. Typically, standards agreed on by the industry are used to quantify them. In the case of scanning wind lidar, no standard has yet been developed, so in this section we explain the uncertainties that we found to be relevant in the context of this study. In Table A1 we show the summary of uncertainty components. Where applicable, the analysis is based on the methods described in IEC-61400-12-1 (2017) and on industry-accepted best practice guidelines (Wagner et al., 2016; Franke, 2018). Each of the individual uncertainty components is explained in the following sections. Some of them are obtained by known procedures, while others are quantified based on procedures we derived

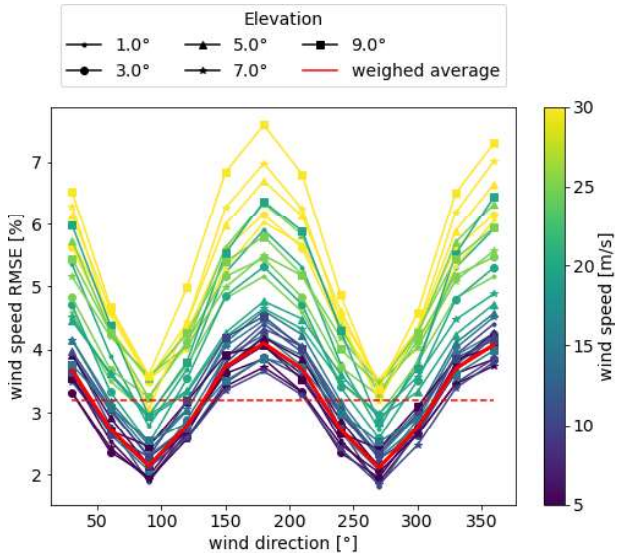

Figure A1. RMSE of simulated VAD. The resulting RMSE is calculated for 100 runs of each combination of parameters as shown in Table A2. Lines in red represent values weighed with the frequency distribution of wind speed and wind direction at the site. The dashed line represents the average of the continuous red line.

specifically for the set-up used in this campaign with a conservative approach.

A1 Calibration

Prior to offshore deployment of the lidar, a calibration of the system was performed using a reference measurement. For this campaign, the calibration of the system was performed according to the calibration procedure for conventional vertical profilers (IEC-61400-12-1, 2017) at UL's test field in Wehlens in northern Germany. This means that we reproduced the measurement performed by a short-range vertical profiler with an elevation angle of 60°. The uncertainties obtained in this way are assumed to be conservative if compared to a line-of-sight calibration, as suggested by Borraccino et al. (2016). This increased uncertainty is due to the large height span and associated wind shear within a single range gate. During the campaign, the maximum elevation angle was closer to 7°, and hence the height range covered by a single range gate is significantly smaller. Accordingly, the actual uncertainty is expected to be smaller than that obtained during the system verification.

A2 Beam positioning

Another uncertainty component is the lidar laser beam positioning, which describes the combined effect of the accuracy of the scanning head in the vertical direction and the vertical wind shear. Here we used scanning lidar precision as given by the manufacturer and used a vertical power-law profile with an exponent $\alpha = 0.14$.

The error of the measurement height due to the curvature of the Earth is considered negligible at the range distance of the measurement location (1.5 km).

A3 Mounting error

The mounting error has been quantified by means of SSL. This has been taken into account in the scanning trajectory design to compensate for it. In this way we almost diminish this error; however there is still a very small remaining error.

A4 Platform vibration

Height variations in the measurement are caused by orientation changes in tilt and roll, due to platform vibration. An analysis of these signals from the internal inclinometer has been performed over the whole campaign. Finally, the effect of wind shear has been evaluated based on an assumption of a power-law profile with an exponent of $\alpha = 0.14$.

A5 Wind field inhomogeneity

The effect of inhomogeneous flow, mainly caused by partial wake effects, has been evaluated based on simulation results from Lundquist et al. (2015). The value is based on the assumption of a wake distance of nine rotor diameters downstream.

A6 Wind speed reconstruction

Additionally, as pointed out in Newsom et al. (2017) with respect to the VAD method, deviations from the perfect sinusoidal occur due to spatial and temporal fluctuations in the velocity field and instrumental errors, and in the context of the VAD algorithm, any departure from the perfect sinusoidal may be regarded as error. Due the lack of a proper physical set-up during this study, numerical simulations have been performed to assess the robustness of the calculation chain of the partial VAD. The results show an average of approximately 3 % mean error due to wind field inhomogeneity on our partial VAD procedure. This can be seen as a conservative estimation of uncertainty in the wind field reconstruction.

The simulations were based on synthetic fields with a defined mean wind speed (U) with superimposed Gaussian random noise $\sigma/U = 10\,\%$. The wind field was scanned with the same geometry as our partial VAD and for all combinations of parameters shown in Table A2.

The results in Fig. A1 show the root-mean-square error (RMSE) of simulations against the reference mean wind speed for 100 runs of each parameter combination. A dependence of the wind field reconstruction on both the azimuth opening angle of the scan trajectory and the wind speed can

Table A1. Summary of uncertainty components that contribute to the global uncertainty of the wind measurement with the scanning lidar and analysis techniques used during this project.

Component	Estimated value [%]	Remark
Calibration (u_1)	1.4–2.2	Conventional calibration as a vertical profiler
Beam positioning (u_2)	0.1	Based on scan head accuracy
Mounting error (u_3)	< 0.1	Accuracy of SSL
Platform vibration (u_4)	1.7	Conservative value from inclinometer variance over the measurement period
Wind field inhomogeneity (u_5)	< 2.5	Conservative value applicable for situations in wake; obtained from Lundquist et al. (2015)
Wind speed reconstruction (u_6)	< 3.0	Conservative value obtained from simulation of our partial VAD

Table A2. Parameter set-up for the VAD simulation.

Parameter	Range	Step
Wind speed (U) [m s^{-1}]	[5, 30]	5
Wind direction [°]	[0, 360]	30
Scanning elevation [°]	[1, 9]	2
Gaussian noise (σ/U) [%]	10	–

be observed. An average value was obtained based on the dependencies and wind speed distribution.

Six sources of uncertainty have been identified that play a role in the overall uncertainty of the lidar wind speed. Assuming that these uncertainties are independent, they can be combined in quadrature to yield

$$u_{\text{lidar}}^2 = u_1^2 + u_2^2 + u_3^2 + u_4^2 + u_5^2 + u_6^2, \tag{A1}$$

and therefore the overall lidar uncertainty in wind speed ranges between 4.4 % and 4.8 %, which is largely dominated by the wind field inhomogeneity and wind speed reconstruction. It is worth noting that these values are very conservative and are expected to be lower in the case of the wind-free sectors.

Appendix B: Weibull probability density function of wind speed scanning lidar per wind sector area

Figure B1 is an extension of Fig. 10 in the main text that shows the probability density function of wind speed scanning lidar per wind sector area using the largest free-wind sector (related to region R5) as reference. The bars shown have a width of 1 m s^{-1}. The height of the bars corresponds to the normalized density function, i.e., the frequency of the measured values contained in a bar multiplied by the bar width.

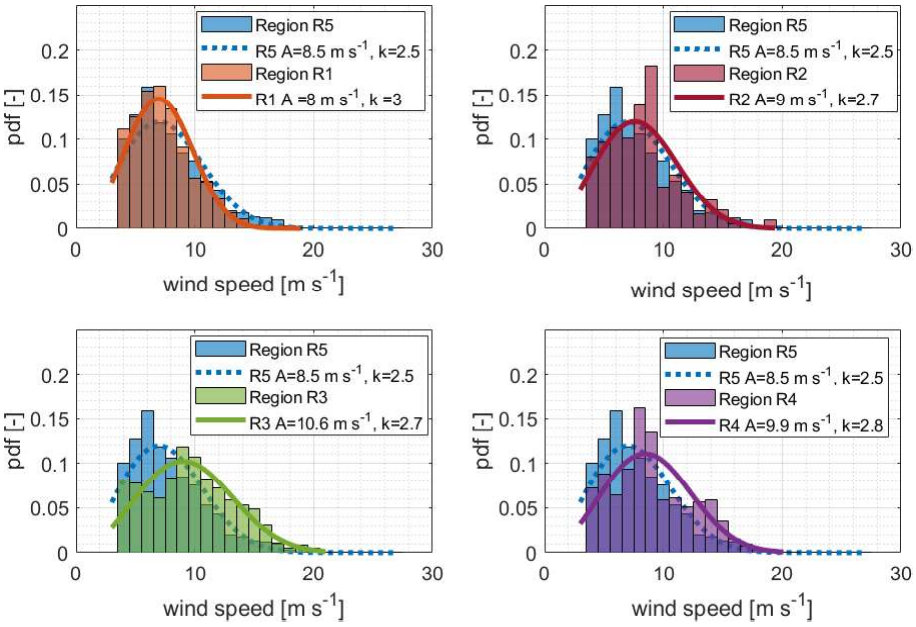

Figure B1. Weibull probability density function (pdf) of wind speed scanning lidar per wind sector area. The sector R5 is used as a reference.

Code and data availability. The airborne data will be published in PANGAEA after the end of the project X-Wakes. The WRF and scanning lidar data will be available upon request after the end of the project X-Wakes, and the mesoscale model itself is open source and can be obtained from https://doi.org/10.5065/D6MK6B4K (NCAR Users Page, 2021). Data from Figs. 12, 14 and 15 are available at https://doi.org/10.6084/m9.figshare.19747252.v1 (Cañadillas, 2022).

Author contributions. BC wrote the manuscript with the support of RF and AL. MB and BC evaluated and prepared most of the figures. JJT together with BC processed the scanning lidar data and wrote the scanning lidar section. MD provided the WRF data and the description of the simulation. TN was involved in the funding acquisition and supervised the research. All authors contributed intensively to an internal review.

Competing interests. The contact author has declared that neither they nor their co-authors have any competing interests.

Disclaimer. Publisher's note: Copernicus Publications remains neutral with regard to jurisdictional claims in published maps and institutional affiliations.

Acknowledgements. The authors would like to thank Rolf Hankers, Thomas Feuerle, Helmut Schulz and Mark Bitter for coordinating and conducting the flight campaigns. Special thanks go to Alexander Tschirch, Hauke Decker and Richard Fruehmann from UL International GmbH for the logistics and installation of the scanning wind lidar. We thank the operator of the wind farm Gode Wind (Oersted) for their support and help with the installation.

Financial support. This research has been performed under the X-Wakes project which has been funded by the Federal Ministry for Economic Affairs and Climate Action (BMWK) under grant number FKZ 03EE3008 (A-G) on the basis of a decision by the German Bundestag.

This open-access publication was funded by Technische Universität Braunschweig.

Review statement. This paper was edited by Johan Meyers and reviewed by two anonymous referees.

References

Ahsbahs, T., Badger, M., Volker, P., Hansen, K. S., and Hasager, C. B.: Applications of satellite winds for the offshore wind farm site Anholt, Wind Energ. Sci., 3, 573–588, https://doi.org/10.5194/wes-3-573-2018, 2018.

Ahsbahs, T., Nygaard, N., Newcombe, A., and Badger, M.: Wind Farm Wakes from SAR and Doppler Radar, Remote Sensing, 12, 462, https://doi.org/10.3390/rs12030462, 2020.

Aitken, M. L., Banta, R. M., Pichugina, Y. L., and Lundquist, J. K.: Quantifying Wind Turbine Wake Characteristics from Scanning Remote Sensor Data, J. Atmos. Ocean. Tech., 31, 765–787, https://doi.org/10.1175/JTECH-D-13-00104.1, 2014.

Akhtar, N., Geyer, B., Rockel, B., Sommer, P. S., and Schrum, C.: Accelerating deployment of offshore wind energy alter wind cli-

mate and reduce future power generation potentials, Sci. Rep., 11, 11826, https://doi.org/10.1038/s41598-021-91283-3, 2021.

Archer, C., Wu, S., ma, Y., and Jimenez, P.: Two Corrections for Turbulent Kinetic Energy Generated by Wind Farms in the WRF Model, Mon. Weather Rev., 148, 4823–4835, https://doi.org/10.1175/MWR-D-20-0097.1, 2020.

Bastine, D., Wächter, M., Peinke, J., Trabucchi, D., and Kühn, M.: Characterizing Wake Turbulence with Staring Lidar Measurements, Journal of Physics: Conference Series, 625, 012006, https://doi.org/10.1088/1742-6596/625/1/012006, 2015.

Cañadillas, B.: Figures wes-2021-159 manuscript, figshare [data set], https://doi.org/10.6084/m9.figshare.19747252.v1, 2022.

Bingöl, F., Mann, J., and Larsen, G. C.: Light detection and ranging measurements of wake dynamics part I: one-dimensional scanning, Wind Energy, 13, 51–61, https://doi.org/10.1002/we.352, 2010.

Borraccino, A., Courtney, M., and Wagner, R.: Generic Methodology for Field Calibration of Nacelle-Based Wind Lidars, Remote Sensing, 8, 6588–6596, https://doi.org/10.3390/rs8110907, 2016.

Brower, M. and Robinson, N.: The OpenWind deep-array wake model: development and validation, Tech. rep., AWS Truepower, Albany, NY, USA, 2012.

BSH: Flächenentwicklungsplan 2020 für die deutsche Nord- und Ostsee, Tech. Rep. 7608, BSH – Bundesamt für Seeschiffahrt und Hydrographie, https://www.bsh.de/DE/THEMEN/Offshore/Meeresfachplanung/Fortschreibung/_Anlagen/Downloads/FEP_2020_Flaechenentwicklungsplan_2020.pdf?__blob=publicationFile&v=6, last access: 1 April 2021.

Cañadillas, B., Foreman, R., Barth, V., Siedersleben, S., Lampert, A., Platis, A., Djath, B., Schulz-Stellenfleth, J., Bange, J., Emeis, S., and Neumann, T.: Offshore wind farm wake recovery: Airborne measurements and its representation in engineering models, Wind Energy, 23, 1249–1265, https://doi.org/10.1002/we.2484, 2020.

Christiansen, M. and Hasager, C.: Wake effects of large offshore wind farms identified from satellite SAR, Remote Sens. Environ., 98, 251–268, https://doi.org/10.1016/j.rse.2005.07.009, 2005.

Corsmeier, U., Hankers, R., and Wieser, A.: Airborne turbulence measurements in the lower troposphere onboard the research aircraft Dornier 128-6, D-IBUF, Meteorol. Z., 10, 315–329, https://doi.org/10.1127/0941-2948/2001/0010-0315, 2001.

Djath, B., Schulz-Stellenfleth, J., and Cañadillas, B.: Impact of atmospheric stability on X-band and C-band synthetic aperture radar imagery of offshore windpark wakes, J. Renew. Sustain. Energ., 10, 043301, https://doi.org/10.1063/1.5020437, 2018.

Donlon, C. J., Martin, M., Stark, J., Roberts-Jones, J., Fiedler, E., and Wimmer, W.: The Operational Sea Surface Temperature and Sea Ice Analysis (OSTIA) system, Remote Sens. Environ., 116, 140–158, https://doi.org/10.1016/j.rse.2010.10.017, 2012.

Dörenkämper, M., Olsen, B. T., Witha, B., Hahmann, A. N., Davis, N. N., Barcons, J., Ezber, Y., García-Bustamante, E., González-Rouco, J. F., Navarro, J., Sastre-Marugán, M., Sīle, T., Trei, W., Žagar, M., Badger, J., Gottschall, J., Sanz Rodrigo, J., and Mann, J.: The Making of the New European Wind Atlas – Part 2: Production and evaluation, Geosci. Model Dev., 13, 5079–5102, https://doi.org/10.5194/gmd-13-5079-2020, 2020.

Emeis, S.: A simple analytical wind park model considering atmospheric stability, Wind Energy, 13, 459–469, https://doi.org/10.1002/we.367, 2010.

Emeis, S.: Wind Energy Meteorology:Atmospheric Physics for Wind Power Generation, Springer International Publishing, 2 edn., https://doi.org/10.1007/978-3-319-72859-9, 2018.

Fischler, M. A. and Bolles, R.: Random sample consensus: a paradigm for model fitting with applications to image analysis and automated cartography, Communications of the ACM, 24, 381–395, https://doi.org/10.1145/358669.358692, 1981.

Fitch, A. C., Olson, J. B., Lundquist, J. K., Dudhia, J., Gupta, A. K., Michalakes, J., and Barstad, I.: Local and mesoscale impacts of wind farms as parameterized in a mesoscale nwp model, Mon. Weather Rev., 140, 3017–3038, https://doi.org/10.1175/MWR-D-11-00352.1, 2012.

Franke, K.: Summary of classification of remote sensing device, type: Leosphere WINDCUBE, techreport PP18030.A1, Deutsche WindGuard Consulting GmbH, Varel, DE, 2018.

Frühmann, R., Neumann, T., and Decker, H.: Platform based infrared sea surface temperature measurement: experiences from a one year trial in the North Sea, in: Deutsche Windenergie-Konferenz (DEWEK), 2018.

Goit, J., Yamaguchi, A., and Ishihara, T.: Measurement and Prediction of Wind Fields at an Offshore Site by Scanning Doppler LiDAR and WRF, Atmosphere, 11, 1–20, https://doi.org/10.3390/atmos11050442, 2020.

Gómez Arranz, P. and Courtney, M.: WP1 – Literature Review: Scanning Lidar For Wind Turbine Power Performance Testing, 2021.

Gottschall, J. and Dörenkämper, M.: Understanding and mitigating the impact of data gaps on offshore wind resource estimates, Wind Energ. Sci., 6, 505–520, https://doi.org/10.5194/wes-6-505-2021, 2021.

Gottschall, J., Catalano, E., Dörenkämper, M., and Witha, B.: The NEWA Ferry Lidar Experiment: Measuring Mesoscale Winds in the Southern Baltic Sea, Remote Sensing, 10, 1620, https://doi.org/10.3390/rs10101620, 2018.

Hahmann, A. N., Sīle, T., Witha, B., Davis, N. N., Dörenkämper, M., Ezber, Y., García-Bustamante, E., González-Rouco, J. F., Navarro, J., Olsen, B. T., and Söderberg, S.: The making of the New European Wind Atlas – Part 1: Model sensitivity, Geosci. Model Dev., 13, 5053–5078, https://doi.org/10.5194/gmd-13-5053-2020, 2020.

Herges, T. G., Maniaci, D. C., Naughton, B. T., Mikkelsen, T., and Sjöholm, M.: High resolution wind turbine wake measurements with a scanning lidar, in: Journal of Physics Conference Series, vol. 854 of Journal of Physics Conference Series, 854, 012021, https://doi.org/10.1088/1742-6596/854/1/012021, 2017.

Hersbach, H., Bell, B., Berrisford, P., Hirahara, S., Horányi, A., Muñoz-Sabater, J., Nicolas, J., Peubey, C., Radu, R., Schepers, D., Simmons, A., Soci, C., Abdalla, S., Abellan, X., Balsamo, G., Bechtold, P., Biavati, G., Bidlot, J., Bonavita, M., De Chiara, G., Dahlgren, P., Dee, D., Diamantakis, M., Dragani, R., Flemming, J., Forbes, R., Fuentes, M., Geer, A., Haimberger, L., Healy, S., Hogan, R. J., Hólm, E., Janisková, M., Keeley, S., Laloyaux, P., Lopez, P., Lupu, C., Radnoti, G., de Rosnay, P., Rozum, I., Vamborg, F., Villaume, S., and Thépaut, J.-N.: The ERA5 global reanalysis, Q. J. Roy. Meteorol. Soc., 146, 1999–2049, https://doi.org/10.1002/qj.3803, 2020.

Huang, H.-P., Giannakopoulou, E.-M., and Nhili, R.: WRF Model Methodology for Offshore Wind Energy Applications, Adv. Meteorol., 2014, 1687–9309, https://doi.org/10.1155/2014/319819, 2014.

IEC-61400-12-1: Wind energy generation systems – Part 12-1: Power performance measurements of electricity producing wind turbines, International Standard IEC TC 29110-1:2016, International Electrotechnical Commission, Geneve, Switzerland, https://webstore.iec.ch/publication/26603 (last access: 10 December 2021), 2017.

Iungo, G. V. and Porté-Agel, F.: Volumetric Lidar Scanning of Wind Turbine Wakes under Convective and Neutral Atmospheric Stability Regimes, J. Atmos. Ocean. Tech., 31, 2035–2048, https://doi.org/10.1175/JTECH-D-13-00252.1, 2014.

Käsler, Y., Rahm, S., Simmet, R., and Kühn, M.: Wake Measurements of a Multi-MW Wind Turbine with Coherent Long-Range Pulsed Doppler Wind Lidar, J. Atmos. Ocean. Tech., 27, 1529–1532, https://doi.org/10.1175/2010JTECHA1483.1, 2010.

Kibona, T. E.: Application of WRF mesoscale model for prediction of wind energy resources in Tanzania, Scientific African, 7, e00302, https://doi.org/10.1016/j.sciaf.2020.e00302, 2020.

Krishnamurthy, R., Reuder, J., Svardal, B., Fernando, H., and Jakobsen, J.: Offshore Wind Turbine Wake characteristics using Scanning Doppler Lidar, Energy Procedia, 137, 428–442, https://doi.org/10.1016/j.egypro.2017.10.367, 2017.

Lampert, A., Bärfuss, K., Platis, A., Siedersleben, S., Djath, B., Cañadillas, B., Hunger, R., Hankers, R., Bitter, M., Feuerle, T., Schulz, H., Rausch, T., Angermann, M., Schwithal, A., Bange, J., Schulz-Stellenfleth, J., Neumann, T., and Emeis, S.: In situ airborne measurements of atmospheric and sea surface parameters related to offshore wind parks in the German Bight, Earth Syst. Sci. Data, 12, 935–946, https://doi.org/10.5194/essd-12-935-2020, 2020.

Larsén, X. G. and Fischereit, J.: A case study of wind farm effects using two wake parameterizations in the Weather Research and Forecasting (WRF) model (V3.7.1) in the presence of low-level jets, Geosci. Model Dev., 14, 3141–3158, https://doi.org/10.5194/gmd-14-3141-2021, 2021.

Lee, J. and Zhao, F.: Global wind report 2021, Tech. rep., Global Wind Energy Council (GWEC), Brussels, Belgium, 2021.

Lundquist, J. K., Churchfield, M. J., Lee, S., and Clifton, A.: Quantifying error of lidar and sodar Doppler beam swinging measurements of wind turbine wakes using computational fluid dynamics, Atmos. Meas. Tech., 8, 907–920, https://doi.org/10.5194/amt-8-907-2015, 2015.

METEK-GmbH: Doppler Lidar Stream Line XR, Brochure, https://metek.de/de/wp-content/uploads/sites/6/2016/01/20150410_DataSheet_StreamLineXR.pdf (last access: 7 February 2022), 2021.

NCAR Users Page: WRF Model User's Page, WRF Version 4.0.1, https://doi.org/10.5065/D6MK6B4K, 2021.

Neumann, T., Nadillas, B. C., Trujillo, J., and Frühmann, R.: MODATA 33 – Meteorologische Messungen N-3.7 und N-3.8, Tech. rep., UL International GmbH, Wilhelmshaven, Germany, 2020.

Newsom, R. K., Brewer, W. A., Wilczak, J. M., Wolfe, D. E., Oncley, S. P., and Lundquist, J. K.: Validating precision estimates in horizontal wind measurements from a Doppler lidar, Atmos. Meas. Tech., 10, 1229–1240, https://doi.org/10.5194/amt-10-1229-2017, 2017.

Nygaard, N. and Newcombe, A.: Wake behind an offshore wind farm observed with dual-Doppler radars, Journal of Physics: Conference Series, 1037, 072008, https://doi.org/10.1088/1742-6596/1037/7/072008, 2018.

Patrick, V., Hahmann, A. N., and Badger, J.: Wake Effects of Large Offshore Wind Farms – a study of the Mesoscale Atmosphere, Ph.D. thesis, DTU Wind Energy, Denmark, 2014.

Platis, A., Bange, J., Bärfuss, K., Cañadillas, B., Hundhausen, M., Djath, B., Lampert, A., Schulz-Stellenfleth, J., Siedersleben, S., Neumann, T., and Emeis, S.: Long-range modifications of the wind field by offshore wind parks – results of the project WIPAFF, Meteorol. Z., 29, 355–376, https://doi.org/10.1127/metz/2020/1023, 2020.

Platis, A., Hundhausen, M., Mauz, M., Siedersleben, S., Lampert, A., Emeis, S., and Bange, J.: The Role of Atmospheric Stability and Turbulence in Offshore Wind-Farm Wakes in the German Bight, Bound.-Lay. Meteorol., 182, 1573–1472, https://doi.org/10.1007/s10546-021-00668-4, 2021.

Pryor, S. C., Shepherd, T. J., Barthelmie, R. J., Hahmann, A. N., and Volker, P.: Wind Farm Wakes Simulated Using WRF, J. Phys.: Conf. Ser., 1256, 012025, https://doi.org/10.1088/1742-6596/1256/1/012025, 2019.

Rettenmeier, A., Schlipf, D., Würth, I., and Cheng, P. W.: Power Performance Measurements of the NREL CART-2 Wind Turbine Using a Nacelle-Based Lidar Scanner, J. Atmos. Ocean. Tech., 31, 2029–2034, https://doi.org/10.1175/JTECH-D-13-00154.1, 2014.

Rott, A., Schneemann, J., Theuer, F., Trujillo Quintero, J. J., and Kühn, M.: Alignment of scanning lidars in offshore wind farms, Wind Energ. Sci., 7, 283–297, https://doi.org/10.5194/wes-7-283-2022, 2022.

Schneemann, J., Rott, A., Dörenkämper, M., Steinfeld, G., and Kühn, M.: Cluster wakes impact on a far-distant offshore wind farm's power, Wind Energ. Sci., 5, 29–49, https://doi.org/10.5194/wes-5-29-2020, 2020.

Schneemann, J., Theuer, F., Rott, A., Dörenkämper, M., and Kühn, M.: Offshore wind farm global blockage measured with scanning lidar, Wind Energ. Sci., 6, 521–538, https://doi.org/10.5194/wes-6-521-2021, 2021.

Siedersleben, S. K., Lundquist, J. K., Platis, A., Bange, J., Bärfuss, K., Lampert, A., Cañadillas, B., Neumann, T., and Emeis, S.: Micrometeorological impacts of offshore wind farms as seen in observations and simulations, Environ. Res. Lett., 13, 1–12, https://doi.org/10.1088/1748-9326/aaea0b, 2018a.

Siedersleben, S. K., Platis, A., Lundquist, J. K., Lampert, A., Bärfuss, K., Canadillas, B., Djath, B., Schulz-Stellenfleth, J., Bange, J., Neumann, T., and Emeis, S.: Evaluation of a Wind Farm Parametrization for Mesoscale Atmospheric Flow Models with Aircraft Measurements, Meteorol. Z., 27, 401–415, https://doi.org/10.1127/metz/2018/0900, 2018b.

Siedersleben, S. K., Platis, A., Lundquist, J. K., Djath, B., Lampert, A., Bärfuss, K., Cañadillas, B., Schulz-Stellenfleth, J., Bange, J., Neumann, T., and Emeis, S.: Turbulent kinetic energy over large offshore wind farms observed and simulated by the mesoscale model WRF (3.8.1), Geosci. Model Dev., 13, 249–268, https://doi.org/10.5194/gmd-13-249-2020, 2020.

Skamarock, W., Klemp, J., Dudhia, J., Gill, D., Liu, Z., Berner, J., Wang, W., Power, J., Duda, M., Barker, D., and Huang, X.-Y.: A description of the advanced research WRF version

3, Technical Report, 162 pages NCAR/TN-556+STR, NCAR - National Center for Atmospheric Research, Boulder, Colorado, USA, https://doi.org/10.5065/1dfh-6p97, 2019.

Smalikho, I. N., Banakh, V. A., Pichugina, Y. L., Brewer, W. A., Banta, R. M., Lundquist, J. K., and Kelley, N. D.: Lidar Investigation of Atmosphere Effect on a Wind Turbine Wake, J. Atmos. Ocean. Tech., 30, 2554–2570, https://doi.org/10.1175/JTECH-D-12-00108.1, 2013.

Sørensen, T. L., Thøgersen, M. L., and Nielsen, P. M.: Adapting and calibration of existing wake models to meet the conditions inside offshore wind farms, EMD International A/S, 2008.

Trujillo, J., Bingöl, F., Mann, J., and Larsen, G. C.: Light detection and ranging measurements of wake dynamics part I: one-dimensional scanning, Wind Energy, 13, 51–61, https://doi.org/10.1002/we.352, 2010.

Volker, P. J. H., Badger, J., Hahmann, A. N., and Ott, S.: The Explicit Wake Parametrisation V1.0: a wind farm parametrisation in the mesoscale model WRF, Geosci. Model Dev., 8, 3715–3731, https://doi.org/10.5194/gmd-8-3715-2015, 2015.

Wagner, R., Courtney, M. S., Pedersen, T. F., and Davoust, S.: Uncertainty of power curve measurement with a two-beam nacelle-mounted lidar, Wind Energy, 19, 1269–1287, https://doi.org/10.1002/we.1897, 2016.

Wang, H. and Barthelmie, R.: Wind turbine wake detection with a single Doppler wind lidar, Journal of Physics: Conference Series, 625, 012017, https://doi.org/10.1088/1742-6596/625/1/012017, 2015.

Werner, C.: Lidar – Range-Resolved Optical Remote Sensing of the Atmosphere, chap. Doppler Wind Lidar, pp. 325–354, Springer-Verlag New York, 2005.

WRF Users Page: WRF Model Physics Options and References, https://www2.mmm.ucar.edu/wrf/users/phys_references.html (last access: 13 July 2020), 2020.

Zhan, L., Letizia, S., and Valerio Iungo, G.: LiDAR measurements for an onshore wind farm: Wake variability for different incoming wind speeds and atmospheric stability regimes, Wind Energy, 23, 501–527, https://doi.org/10.1002/we.2430, 2020.